The Astrophysical Journal, 835:286 (15pp), 2017 February 1 doi:10.3847/1538-4357/835/2/286
© 2017. The American Astronomical Society. All rights reserved.

Extremely Red Submillimeter Galaxies: New $z \gtrsim 4$–6 Candidates Discovered Using ALMA and Jansky VLA

Soh Ikarashi[1], R. J. Ivison[2,3], Karina I. Caputi[1], Kouichiro Nakanishi[4,5], Claudia D. P. Lagos[6,7], M. L. N. Ashby[8], Itziar Aretxaga[9], James S. Dunlop[2], Bunyo Hatsukade[10], David H. Hughes[9], Daisuke Iono[4,5], Takuma Izumi[10], Ryohei Kawabe[4,5], Kotaro Kohno[10,11], Kentaro Motohara[10], Kouji Ohta[12], Yoichi Tamura[10], Hideki Umehata[10,13], Grant W. Wilson[14], Kiyoto Yabe[15], and Min S. Yun[14]

[1] Kapteyn Astronomical Institute, University of Groningen, P.O. Box 800, 9700 AV Groningen, Netherlands; sikarash@astro.rug.nl
[2] Institute for Astronomy, University of Edinburgh, Royal Observatory, Blackford Hill, Edinburgh EH9 3HJ, UK
[3] European Southern Observatory, Karl Schwarzschild Str. 2, D-85748 Garching, Germany
[4] National Astronomical Observatory of Japan, Mitaka, Tokyo 181-8588, Japan
[5] SOKENDAI (The Graduate University for Advanced Studies), Shonan Village, Hayama, Kanagawa 240-0193, Japan
[6] Australian Research Council Centre of Excellence for All-sky Astrophysics (CAASTRO), 44 Rosehill Street, Redfern, NSW 2016, Australia
[7] International Centre for Radio Astronomy Research, University of Western Australia, 7 Fairway, Crawley 6009, Perth WA, Australia
[8] Harvard-Smithsonian Center for Astrophysics, 60 Garden Street, Cambridge, MA 02138, USA
[9] Instituto Nacional de Astrofísica, Óptica y Electrónica (INAOE), Aptdo. Postal 51 y 216, 72000 Puebla, Mexico
[10] Institute of Astronomy, University of Tokyo, 2-21-1 Osawa, Mitaka, Tokyo 181-0015, Japan
[11] Research Center for the Early Universe, School of Science, University of Tokyo, 7-3-1 Hongo, Bunkyo, Tokyo 113-0033, Japan
[12] Department of Astronomy, Kyoto University, Kitashirakawa-Oiwake-Cho, Sakyo-ku, Kyoto 606-8502, Japan
[13] The Open University of Japan, 2-11 Wakaba, Mihama-ku, Chiba 261-8586, Japan
[14] Department of Astronomy, University of Massachusetts, Amherst, MA 01003, USA
[15] Kavli Institute for the Physics and Mathematics of the Universe (WPI), The University of Tokyo, 5-1-5 Kashiwanoha, Kashiwa, Chiba 277-8583, Japan
Received 2016 August 26; revised 2016 December 16; accepted 2016 December 29; published 2017 February 2

Abstract

We present the detailed characterization of two extremely red submillimeter galaxies (SMGs), ASXDF1100.053.1 and 231.1, with the Atacama Large Millimeter/submillimeter Array (ALMA) and the Jansky Very Large Array. These SMGs were originally selected using AzTEC at 1100 μm, and are observed by *Herschel* to be faint at 100–500 μm. Their (sub)millimeter colors are as red as—or redder—than known $z \gtrsim 5$ SMGs; indeed, ASXDF1100.053.1 is redder than HFLS 3, which lies at $z = 6.3$. They are also faint and red in the near-/mid-infrared: $\sim$1 μJy at IRAC 4.5 μm and <0.2 μJy in the K_s filter. These SMGs are also faint in the radio waveband, where $F_{6\text{GHz}} = 4.5\,\mu$Jy for ASXDF1100.053.1 and $F_{1.4\text{GHz}} = 28\,\mu$Jy for ASXDF1100.231.1, suggestive of $z = 6.5^{+1.4}_{-1.1}$ and $z = 4.1^{+0.6}_{-0.7}$ for ASXDF1100.053.1 and 231.1, respectively. ASXDF1100.231.1 has a flux excess in the 3.6 μm filter, probably due to Hα emission at $z = 4$–5. Derived properties of ASXDF1100.053.1 for $z = 5.5$–7.5 and 231.1 for $z = 3.5$–5.5 are as follows: their infrared luminosities are $[6.5 - 7.4] \times 10^{12}$ and $[4.2\text{–}4.5] \times 10^{12}\,L_\odot$; their stellar masses are $[0.9\text{–}2] \times 10^{11}$ and $[0.4\text{–}3] \times 10^{10}\,M_\odot$; their circularized half-light radii in the ALMA maps are $\sim$1 and $\lesssim$0.2 kpc ($\sim$2–3 kpc for 90% of the total flux). Last, their surface infrared luminosity densities, Σ_{IR}, are $\sim 1 \times 10^{12}$ and $\gtrsim 1.5 \times 10^{13}\,L_\odot$ kpc^{-2}, similar to values seen for local (U)LIRGs. These data suggest that ASXDF1100.053.1 and 231.1 are compact SMGs at $z \gtrsim 4$ and can plausibly evolve into $z \gtrsim 3$ compact quiescent galaxies.

Key words: galaxies: evolution – galaxies: formation – galaxies: high-redshift – submillimeter: galaxies

1. Introduction

Submillimeter (submm) galaxies (SMGs) with infrared (IR, rest-frame 8–1000 μm) luminosities, $L_{\text{IR}} \gtrsim 10^{12}\,L_\odot$, are routinely detected in deep continuum images at $\lambda_{\text{obs}} = 850$–1300 μm using ground-based single-dish telescopes. Even out to $z \sim 7$, there is no significant loss of sensitivity to these SMGs, given the strong negative K correction in the Rayleigh–Jeans tail of their dust spectral energy distributions (SEDs) (e.g., Blain et al. 2002).

Despite 20 years of deep submm surveys since Smail et al. (1997), our knowledge of the upper half of the redshift distribution of SMGs remains incomplete. Early attempts to determine redshifts were conducted toward SMGs with radio counterparts because low-resolution (sub)mm images obtained with single dishes require high-resolution radio continuum maps from radio interferometers such as the Karl G. Jansky Very Large Array (VLA) in order to pinpoint source positions (Ivison et al. 1998, 2000, 2002, 2005, 2007; Smail et al. 1999; Borys et al. 2004; Pope et al. 2006; Aretxaga et al. 2011; Biggs et al. 2011; Yun et al. 2012; Umehata et al. 2014). Intensive studies of radio-bright SMGs were able to yield spectroscopic redshifts for those out to $z \sim 3$ (e.g., Chapman et al. 2003, 2005). However, at that time, radio sensitivities could not detect SMGs beyond $z \sim 3$, and as many as half of the SMGs lacked reliable radio counterparts (see e.g., Ivison et al. 2007; Biggs et al. 2011, cf. Lindner et al. 2011). Later attempts to determine SMG positions and redshifts using near- and mid-IR imaging could not fully overcome the bias toward lower redshifts, since the K corrections there are no more favorable than those in the radio regime, such that high-redshift sources are much fainter (e.g., Wardlow et al. 2011; Yun et al. 2012). Millimeter (mm) spectroscopic surveys toward gravitationally lensed dusty star-forming galaxies, taking advantage of their apparent ultra brightness, revealed a redshift distribution stretching out to $z \sim 5.8$ (e.g., Vieira et al. 2013; Weiß et al. 2013; Strandet et al. 2016). These surveys suggested a larger fraction of SMGs at $z \gtrsim 3$ than previous studies of unlensed

SMGs, perhaps partly because they were selected at 1.3 mm rather than the traditional 0.8–1.1 mm, but also because the requirement for high magnification favors galaxies with a long line of sight. We need to reveal the intrinsic redshift distributions of unlensed SMGs in large contiguous maps to determine their abundance in the early Universe and to study the evolution of the most massive galaxies via abundance matching with other populations, and with cosmological predictions (e.g., Hayward et al. 2013; Cowley et al. 2015).

Early (sub)mm interferometric imaging of intrinsically bright SMGs, conducted with the IRAM Plateau de Bure interferometer (PdBI) and the Submillimeter Array (SMA) (e.g., Gear et al. 2000; Iono et al. 2006; Younger et al. 2007; Dannerbauer et al. 2008; Younger et al. 2009), pinpointed the positions of SMGs, including radio-faint ones, and resulted in the discovery of SMGs at $z \gtrsim 4$–5 (e.g., Capak et al. 2011). Subsequently, surveys with PdBI and the Combined Array for Research in Millimeter-wave Astronomy indicated that the redshift distribution of intrinsically bright SMGs most likely stretches to $z \sim 6$ (Smolčić et al. 2012).

The capabilities of the Atacama Large Millimeter/submm Array (ALMA) now enable astronomers to rapidly pinpoint the positions of large samples of SMGs, with no strong biases (although see Zhang et al. 2016). ALMA submm continuum imaging surveys toward LABOCA 870 μm-selected SMGs (e.g., Hodge et al. 2013; Simpson et al. 2014) and AzTEC 1100 μm-selected SMGs (Ikarashi et al. 2015) have uncovered a number of radio-faint SMGs. Some of these radio-faint SMGs have been too faint at optical/near-IR wavelengths to permit estimation of their redshifts using standard techniques (Simpson et al. 2014; Ikarashi et al. 2015). Some could lie at very high redshifts, i.e., $z \gtrsim 5$; alternatively, they could be heavily dust-obscured SMGs at more moderate redshifts, $z \approx 3$–5. The redshifts of these SMGs remain a puzzle, with important implications for our understanding of early galaxy evolution.

ALMA mm-wave continuum imaging of $z \gtrsim 3$ candidate SMGs have revealed surprisingly compact sizes, supporting the idea that $z \gtrsim 3$ SMGs could evolve into compact quiescent galaxies at $z \sim 2$ (Ikarashi et al. 2015). The latest intensive optical, near-, and mid-IR extragalactic surveys have reported compact quiescent galaxies up to $z \sim 4$ (Straatman et al. 2015). In order to understand the formation phase of these massive passive galaxies at $z \gtrsim 3$, surveys and studies of SMGs $z \gtrsim 4$–5 are as important today as they ever were.

In this paper, we present a detailed multiwavelength analysis of two ALMA-identified galaxies, ASXDF1100.053.1 and ASXDF1100.231.1, detected originally in a deep ASTE/AzTEC survey at 1100 μm (Ikarashi et al. 2015). These SMGs were selected for further scrutiny on the basis of their secure non-detections in *Herschel* 100–500 μm images, which give the most useful constraints on redness at submm wavelengths (see also Cox et al. 2011; Riechers et al. 2013; Dowell et al. 2014; Asboth et al. 2016; Ivison et al. 2016; Mancuso et al. 2016). Because they are too faint at optical and near-IR wavelengths to allow meaningful estimation of their redshifts using classical photometric techniques, we have instead determined photometric redshifts using deep radio, submm, and far-IR images from the Janksy VLA, ALMA, SCUBA-2, and *Herschel*, respectively, aiming to reveal whether these galaxies are indeed located at very high redshifts—obvious candidate progenitors of the massive passive galaxies at $z \gtrsim 3$.

We adopt a cosmology with $H_0 = 70$ km s^{-1} Mpc^{-1}, $\Omega_M = 0.3$, and $\Omega_\Lambda = 0.7$ throughout, and all magnitudes refer to the AB system.

2. The Targets: ASXDF1100.053.1 and 231.1

ASXDF1100.053.1 and 231.1 are the brightest and second-brightest 1100 μm-selected ALMA-identified SMGs among the $z \gtrsim 3$ candidates discovered in our ALMA Cycle-1 program (2012.1.00326.S: PI. Ikarashi). The parent sample consists of 221 SMGs discovered in a deep AzTEC/ASTE 1100 μm map covering 950 arcmin^2 of the Subaru/*XMM-Newton* Deep Field (SXDF) (e.g., Furusawa et al. 2008), which includes the UKIRT IR Deep Sky Survey (UKIDSS) Ultra Deep Survey (UDS) field (e.g., Lawrence et al. 2007). In our ALMA program, we targeted 30 SMGs from this parent sample, selected on the basis of their faintness in 1.4 GHz VLA imaging ($5\sigma \lesssim 35$ μJy, V. Arumugam et al. 2017, in preparation) and SPIRE 250 μm images ($3\sigma_{\rm confusion} \lesssim 18.3$ mJy, Oliver et al. 2012), aiming to reveal the tail of the SMG redshift distribution. The faintness of these two SMGs at optical, near-, and mid-IR wavelengths suggests $z \gtrsim 4$–5 (Ikarashi et al. 2015; Figure 1). The submm (250, 350, 500, and 850 μm)/mm (1100 μm)/radio (1.4 GHz) colors of ASXDF1100.053.1 and 231.1 are as red as—or redder—than known $z \gtrsim 5$ SMGs, which suggests that these new SMGs could lie at $z \gtrsim 5$ (Figure 1). We therefore focus on these two SMGs for a pilot study of candidate extremely high-redshift SMGs.

3. Data and Photometry

Here we describe the observational data used in this paper. Our images are shown in Figures 2 and 3, and measurements are listed in Table 1.

3.1. ALMA 1100 μm Continuum

We first describe the ALMA data taken in Cycle 1 (S. Ikarashi et al. 2017, in preparation: see also Ikarashi et al. 2015). These observations were carried out with an array configuration similar to C32-3, with 25 working 12 m antennas covering *uv* distances up to ∼400 kλ. On-source observation times (per target) were 3.6–4.5 minutes.

The two SMGs were also observed as part of an ALMA continuum imaging survey of 333 bright AzTEC SMGs in Cycle 2 (2013.1.00781: PI. Hatsukade). These observations were carried out in array configurations C34-5 and C34-7, with 37–38 working 12 m antennas covering *uv* distances up to ∼1500 kλ. On-source observation times per source were 0.6 minutes.

We combined the ALMA data obtained in Cycles 1 and 2. Synthesized beams were then $0''.46 \times 0''.35$ (PA, 69°) and $0''.57 \times 0''.48$ (PA, 82°) for ASXDF1100.053.1 and 231.1, respectively, with sensitivities of 70 and 63 μJy beam^{-1} (1σ). ASXDF1100.053.1 and 231.1 were detected with $S_{\rm peak}/N = 27$ and 29, respectively, with total flux densities $F_{1100\mu m} = 3.51 \pm 0.15$ and 2.28 ± 0.08 mJy.

Both ASXDF1100.053.1 and 231.1 appear to be single unblended SMGs, with no signs of multiplicity; their ALMA 1100 μm flux densities are consistent (within 1σ) with those measured by AzTEC/ASTE (S. Ikarashi et al. 2017, in preparation).

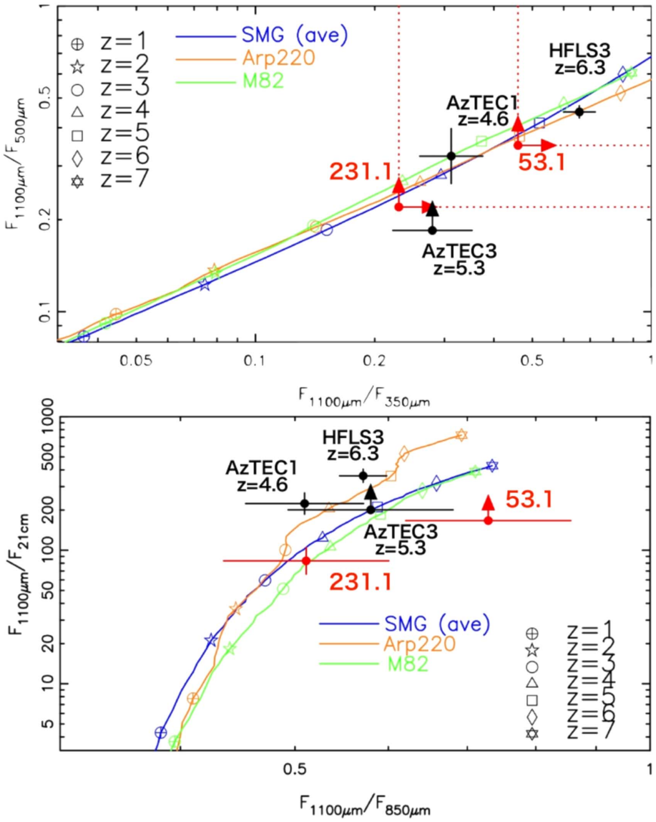

Figure 1. Comparison of submm/mm/radio colors for ASXDF1100.053.1 and 231.1 with colors of known $z \gtrsim 5$ SMGs from the literature. Submm/mm/radio colors for ASXDF1100.053.1 and 231.1 are marked by red crosses or arrows based on fluxes in Table 1. The SMGs with the highest known redshift, HFLS3 at $z = 6.3$ (Riechers et al. 2013), and known $z \sim 5$ SMGs, AzTEC1 and AzTEC 3 (Smolčić et al. 2015), are marked by black points. The blue, orange, and green lines mark the color track as a function of redshift of the average SED of 99 ALMA-identified SMGs (Swinbank et al. 2014) and SED templates of Arp 220 and M 82 (Silva et al. 1998), respectively.

3.2. Jansky Very Large Array Radio Continuum

3.2.1. Classic VLA 1.4 GHz Continuum

The accurate SMG positions from our ALMA images enable us to exploit existing deep VLA radio continuum maps. ASXDF1100.231.1 was detected at 3.3σ in an existing wide deep VLA 1.4 GHz image of the SXDF field (V. Arumugam et al. 2017, in preparation et al. 2016); ASXDF1100.053.1 was not detected. The rms noise of the map is 6–8 μJy beam^{-1}, and the FWHM synthesized beam is $\sim$1$''$.5.

3.2.2. Jansky VLA 6 GHz Continuum

In order to measure the radio flux density of ASXDF1100.053.1, we conducted new extremely deep Jansky VLA observations. The data were obtained from 2015 February to April with the Jansky VLA in its B configuration, using the new three-bit samplers[16], with the WIDAR correlator, covering an almost contiguous 4 GHz band across 4–8 GHz (several spectral windows covering a total of $\approx$0.25 GHz were discarded due to radio-frequency interference). The phase center was set to be the position of ASXDF1100.053.1. The FWHM field of view covers a circular area of radius 3.7 arcmin in the final map. The total observation time was 14 hr, of which 10.1 hr were spent on-source. We chose J0239−0234 as the gain calibrator, using 3C 48 as the bandpass calibrator and to set the flux density scale. We reduced the data with CASA and imaged using a natural weighting scheme. The resulting map reaches an rms noise level of 1.1 μJy beam^{-1} and has a synthesized beam size of 1$''$.5 × 1$''$.2 (PA, 16°.2). Given the color correction between $\nu_{\rm obs} = 1.4$ and 6 GHz for a radio spectral index, $\alpha = -0.8$, the sensitivity of the new Jansky VLA 6 GHz map is more than twice deeper than the old VLA 1.4 GHz map. In the new 6 GHz map we detect emission at the position of ASXDF1100.053.1: 4.5 ± 1.1 μJy (4.0 σ). The source characteristics are summarized in Table 2.

3.3. Herschel/SPIRE 250–500 μm Continuum

We use the *Herschel*/SPIRE 250, 350, and 500 μm maps in the UKIDSS UDS field, provided as part of the HerMES (Oliver et al. 2012) second data release (DR2). Armed with ALMA positions, accurate to $<0''.1$, it is clear that neither ASXDF1100.053.1 nor 231.1 were detected in deep imaging by *Herschel* PACS and SPIRE images (see Figures 2 and 3): the respective flux densities in the 250, 350, and 500 μm maps are 4.2, 6.3, and 9.5 mJy beam^{-1}, and the flux densities at the position of ASXDF1100.231.1 are 0.7, 5.2, and 3.1 mJy beam^{-1}. These values are below the 3σ limits measured in residual SPIRE maps of $5' \times 5'$ areas around ASXDF1100.053.1 and 231.1, where the sources in the residual maps have been deblended based on the positions of known VLA 1.4 GHz and MIPS 24 μm sources. The respective 250, 350, and 500 μm flux densities of ASXDF1100.053.1 in the residual images are −1.3, 0.1, and 4.3 mJy beam^{-1}, and the flux densities of ASXDF1100.231.1 are 0.6, 4.0, and 0.8 mJy beam^{-1}.

3.4. SCUBA-2 850 μm Continuum

Both ASXDF1100.053.1 and 231.1 are detected in the deep SCUBA-2 850 μm map of the SCUBA-2 Cosmology Legacy Survey Data Release 1. Geach et al. (2017) referred to them as UDS0186 and UDS0206, with 850 μm flux densities of 4.8 ± 1.1 and 4.5 ± 1.1 mJy, respectively. The respective offsets between their ALMA 1100 μm and SCUBA-2 850 μm positions are 2.5 and 5.7 arcsec, consistent with the SCUBA-2 positional offset distributions (Simpson et al. 2015b).

3.5. Spitzer mid-IR Continuum

We use the deep *Spitzer* IRAC 3.6 and 4.5 μm maps from the *Spitzer* Extended Deep Survey (Ashby et al. 2013) and IRAC 5.8 and 8.0 μm and MIPS 24 μm data from the *Spitzer* UKIDSS Ultra Deep Survey (PI. J. Dunlop; see, e.g., Caputi et al. 2011). IRAC counterparts of ASXDF1100.053.1 and 231.1 were found at (R.A., decl.) = (02$^{\rm h}$16$^{\rm m}$48$^{\rm s}$.19, −04°58$'$59$''$.6) and (02$^{\rm h}$17$^{\rm m}$59$^{\rm s}$.62, −04°46$'$59$''$.7), respectively, with offsets from the ALMA positions of 0$''$.2 and 0$''$.5. Photometric measurements performed at the IRAC positions with fixed apertures and aperture corrections for 2$''$.4-ϕ(IRAC 3.6 and 4.5 μm); 2$''$.8-ϕ (IRAC 5.8 and 8.0 μm). The MIPS 24 μm upper limit (3σ) is based on photometry at random positions including an aperture correction for 7$''$$\phi$. For $<2\sigma$ detections in IRAC maps, we adopt 2σ upper limits.

[16] We acknowledge funding toward the three-bit samplers used in this work from ERC Advanced Grant 321302, COSMICISM.

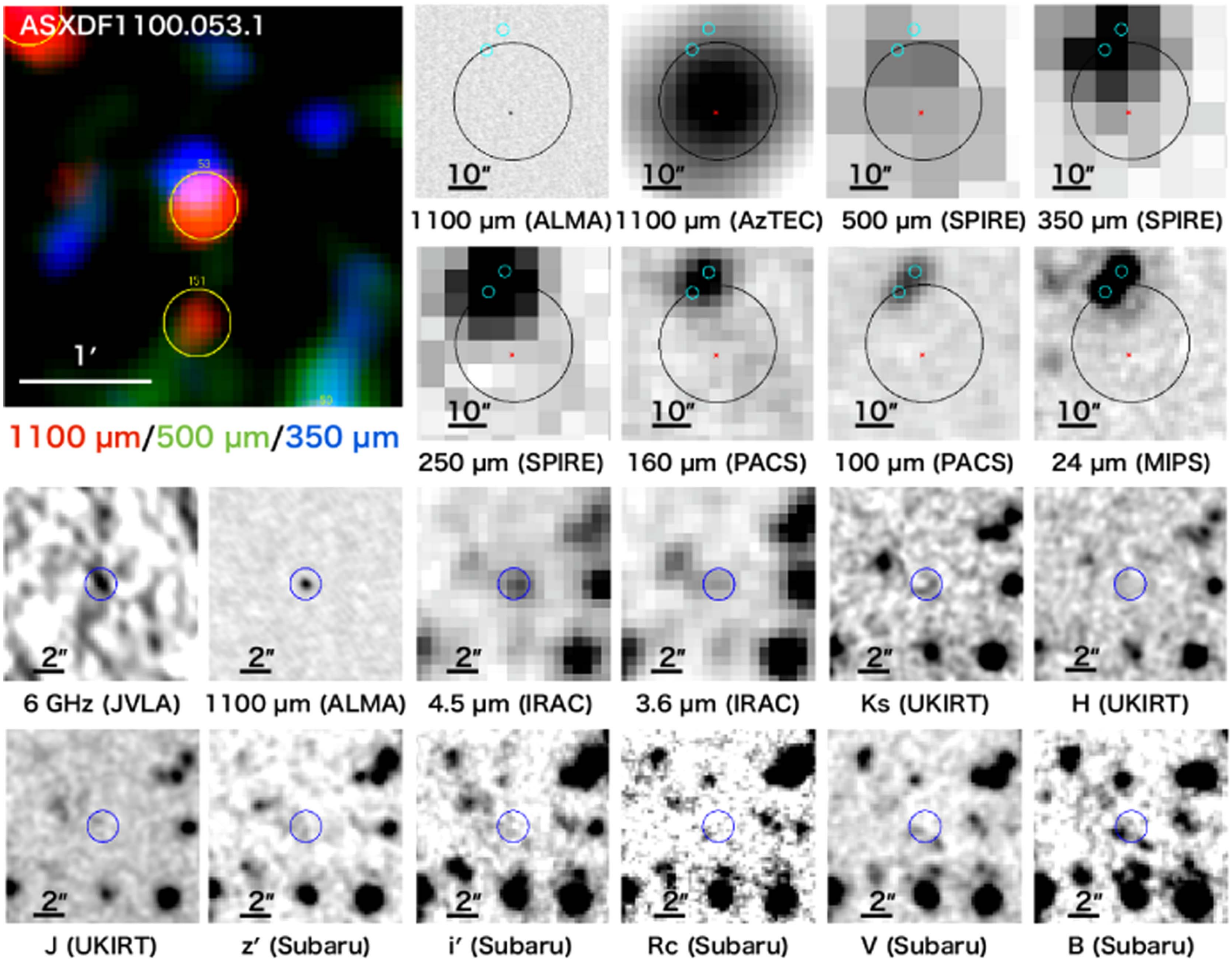

Figure 2. Multiwavelength images of ASXDF1100.053.1. Top right: RGB image (R, G, and B being 1100, 500, and 350 μm, respectively) around ASXDF1100.053.1. Yellow circles mark AzTEC 1100 μm sources. First and second rows from top: ALMA, AzTEC, SPIRE, PACS, and *Spitzer* images. The black circle marks the AzTEC position of ASXDF1100.053.1 and the beam size of the AzTEC/ASTE image (30″). The red cross marks the ALMA position of ASXDF1100.053.1. The small cyan circle marks the position of a *Spitzer* and *Herschel* bright source near ASXDF1100.053.1. Third and fourth rows from top: Jansky VLA, ALMA, IRAC, UKIRT, and Subaru images of ASXDF1100.053.1. The blue circle marks the ALMA position of ASXDF1100.053.1.

3.6. Optical/Near-IR Continuum

We use optical/near-IR images at B, V, Rc, i', and z' bands from the Subaru Telescope (Furusawa et al. 2008) and near-IR images at J, H, and K_s bands from the UKIDSS (Lawrence et al. 2007). We measured fluxes with fixed apertures at the positions of the IRAC counterparts and applied aperture corrections: $2''\phi$ aperture for B through K_s. Errors were derived from random aperture photometry. Again, for $<2\sigma$ detections, we adopt 2σ upper limits.

4. Radio/Millimeter-wave Photometric Redshifts

The existence of SMGs that are extremely faint at optical to mid-IR wavelengths has long been recognized (e.g., Hughes et al. 1998; Ivison et al. 2000; Wang et al. 2009; Weiß et al. 2009; Walter et al. 2012), and radio/submm colors have been used to estimate the redshifts of heavily dust-obscured SMGs (e.g., Carilli & Yun 1999; Hughes et al. 2002; Ivison et al. 2005; Aretxaga et al. 2003, 2005, 2007), exploiting the tight correlation between radio and far-IR luminosities that is seen for local galaxies (Condon 1992).

4.1. Method

We estimate the radio/submm photometric redshifts of ASXDF1100.053.1 and ASXDF1100.231.1 by fitting dust SED templates to ALMA 1100 μm, SCUBA-2 850 μm, and (J) VLA 6 or 1.4 GHz flux densities.

Obtaining strong constraints around the peak of the dust SEDs is important for radio and (sub)mm photometric redshift estimates to exclude spurious SED models that return dubious redshift estimates because of the degeneracy between redshift and dust temperature (e.g., Blain et al. 2002). For most SMGs at $z \approx 2$–3, the *Herschel* SPIRE images at 250, 350, and 500 μm cover the redshifted dust SED peak. ASXDF1100.053.1 and 231.1 are not detected in the *Herschel* SPIRE maps (Figures 2 and 3), and we therefore included 3σ upper limits from the SPIRE data at 250, 350, and 500 μm as survival functions (Isobe et al. 1986), as was done for SCUBA 450 μm upper limits in radio/submm photometric redshift estimates in Aretxaga et al. (2007). The survival function enables us to derive redshift probability densities throughout an entire redshift range and avoid drastic changes that are due to upper limits in fluxes.

Radio/submm photometric redshifts typically have larger uncertainties than optical/near-IR photometric redshifts because

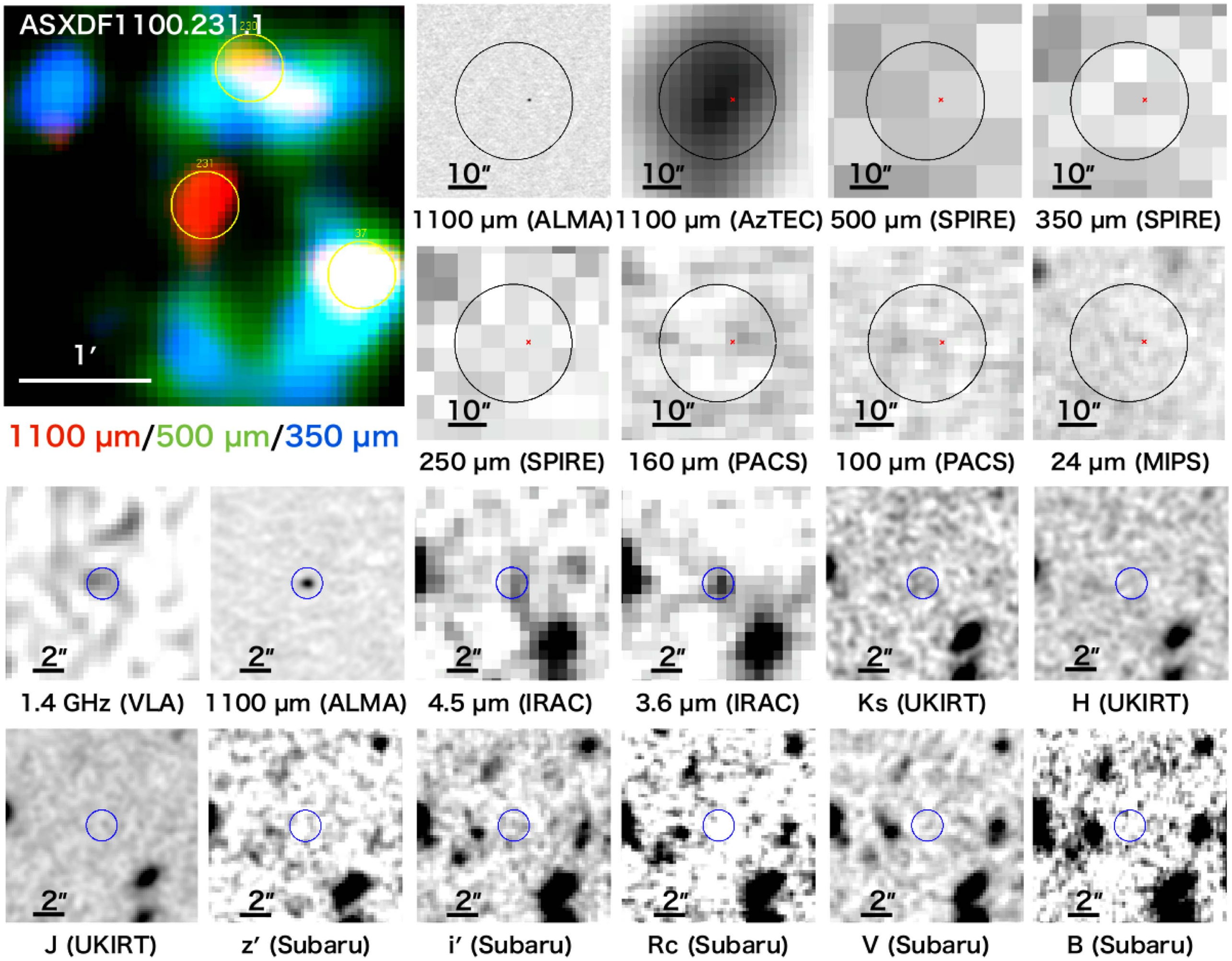

Figure 3. Multiwavelength images of ASXDF1100.231.1.

they lack clear SED features, such as continuum breaks. Since redshift estimates using radio/(sub)mm colors depend on the adopted dust SED, we need to use SEDs representative of our target population, i.e., galaxies with similar IR luminosities and similar redshifts.

Here, we adopt the SED template made from of 99 ALMA-identified SMGs, derived from deep *Herschel* and ALMA submm and VLA radio data presented in Swinbank et al. (2014). The SEDs of ALMA-identified SMGs were fit with a library of 185 SEDs from Chary & Elbaz (2001), Rieke et al. (2009), Draine et al. (2007), Ivison et al. (2010), and Carilli et al. (2011), adopting optical/near-IR photometric redshifts from Simpson et al. (2014). The dust temperature of the best-fit SED of each ALMA-identified SMG is listed in the paper. We randomly picked SEDs from the parent SED library along with the dust temperature distribution (19–52 K) for the ALMA-identified SMGs derived in Swinbank et al. (2014),[17] and calculated the redshift probability density distribution for each chosen SED. We bootstrapped this process and combined the derived probability density distributions in order to achieve a redshift probability density distribution weighted by the likelihood of each SED temperature.

[17] The reformatted SED templates with dust temperatures used in Swinbank et al. (2014) are distributed at http://astro.dur.ac.uk/~ams/HSOdeblend/templates/.

The multivariate Gaussian probability distribution, Φ, for k colors is given by

$$\Phi(\boldsymbol{c}_i - \boldsymbol{c}_0) = (2\pi)^{-k/2}|\boldsymbol{A}^{-1}|^{1/2} \times \exp\left(-\frac{1}{2}(\boldsymbol{c}_i - \boldsymbol{c}_0)'\boldsymbol{A}^{-1}(\boldsymbol{c}_i - \boldsymbol{c}_0)\right)\prod_{\nu} \mathrm{Surv}, \quad (1)$$

where $\boldsymbol{A}$ is a covariance matrix. Here we assume that any non-diagonal elements in the covariance matrix are zero, therefore $(\boldsymbol{c}_i - \boldsymbol{c}_0)'\boldsymbol{A}^{-1}(\boldsymbol{c}_i - \boldsymbol{c}_0)$ can be substituted by standard χ^2. Surv is a survival function (Isobe et al. 1986). The survival function is expressed using an complementary error function as

$$\mathrm{Surv} = \frac{1}{\sqrt{2\pi}}\int_{(c_i(\lambda)-c_{\mathrm{obs}}(\lambda))/\sigma_{\mathrm{obs}}}^{\infty} e^{-t^2/2}dt. \quad (2)$$

We assume that the flux density errors follow Gaussian distributions. The final redshift probability distribution, $P(z)$, of any galaxy is the sum of the individual probabilities from the SEDs, or explicitly

$$P(z) = a\sum_{i,\forall z}\Phi(\boldsymbol{c}_i - \boldsymbol{c}_0), \quad (3)$$

where a is the normalization constant, such that $\int_0^{z_{\max}} P(z) = 1$, where $z_{\max} = 10$. The asymmetric error bars $(z_-,\ z_+)$

Table 1
Photometric Data of ASXDF1100.053.1 and 231.1

Wavelength	ASXDF1100.053.1 Flux (μJy)	ASXDF1100.231.1 Flux (μJy)	Reference
Suprime Cam *B* band (0.45 μm)	<0.014	<0.016	1
Suprime Cam *V* band (0.55 μm)	<0.023	<0.021	1
Suprime Cam *Rc* band (0.66 μm)	<0.027	<0.025	1
Suprime Cam *i'* band (0.77 μm)	<0.027	<0.025	1
Suprime Cam *z'* band (0.92 μm)	0.067 ± 0.036	<0.064	1
WFCAM *J* band (1.2 μm)	<0.14	<0.14	2
WFCAM *H* band (1.6 μm)	<0.23	<0.23	2
WFCAM K_s (2.2 μm)	<0.19	<0.19	2
IRAC 3.6 μm	0.61 ± 0.14	1.00 ± 0.17	3
IRAC 4.5 μm	1.43 ± 0.17	0.93 ± 0.22	3
IRAC 5.8 μm	3.5 ± 1.9	<3.5	4
IRAC 8.0 μm	<4.7	7.4 ± 2.6	4
MIPS 24 μm	<66	<66	4
PACS 110 μm	<2400	<2400	5
PACS 160 μm	<5000	<5000	5
SPIRE 250 μm	<9600	<8800	5
SPIRE 350 μm	<7700	<9800	5
SPIRE 500 μm	<10000	<10000	5
SCUBA-2 850 μm	4800 ± 1100	4500 ± 1100	6
ALMA 1100 μm	3510 ± 150	2280 ± 80	7
JVLA 6 GHz	4.46 ± 1.1	⋯	7
VLA 1.4 GHz	<17.8	27.6 ± 8.7	8

Note. 2σ and 3σ upper limits are presented for (stellar) emission at 0.45–8.0 μm and dust/synchrotron emission at 24 μm through 1.4 GHz, respectively.

References. (1) Furusawa et al. (2008); (2) Lawrence et al. (2007); (3) Ashby et al. (2013); (4) Caputi et al. (2011); (5) Oliver et al. (2012); (6) Geach et al. (2017); (7) this work; (8) V. Arumugam et al. 2017, in preparation.

Table 2
JVLA Observations

Observation date	2015 Feb 16 Mar 2, 9, 17, and 30 Apr 2
Frequency	4–8 GHz
Phase center (J2000)	R.A. = $02^{\rm h}16^{\rm m}48^{\rm s}$ Decl. = −04°58′59″
Gain calibrator	J0239−0234
Flux density calibrator	3C 48
Bandpass calibrator	3C 48
Array configuration	B
Projected baselines	0.2–11 km
Primary beam	7.3 arcmin (FWHM) at 6 GHz
Synthesized beam size	1″5 × 1″1 (PA, 16°2)
Map noise level	1.1 μJy beam^{-1}

correspond to 68% confidence levels such that $\int_{z_-}^{z_+} P(z)\, dz = 0.68$ and $(z_+ - z_-)$ is minimized. These calculations follow the methodology presented in Hughes et al. (2002) and that on the survival function.

4.2. Resulting Redshift Estimates

The radio/submm photometric redshift probability distributions for ASXDF1100.053.1 and 231.1 are shown with black curves in Figure 4 along with fit SEDs. The resulting photometric redshifts for ASXDF1100.053.1 and 231.1 are $6.5^{+1.4}_{-1.1}$ and $4.1^{+0.6}_{-0.7}$, respectively.

Probability densities, Φ, for each SED with $T_d = 19$, 32, and 52 K given by Equation (1) are shown at the bottom of Figure 4, with the aim of understanding the contributions of these SEDs to the combined photometric redshift probability distributions. The Φ density plots indicate that the low probabilities of low-redshift solutions in the combined redshift probability distribution, $P(z)$, are due to two factors: (1) cold SEDs are rare, which is due to the dust temperature distribution, and (2) cold SEDs give poor fits. The Φ plots also demonstrate that solutions for cold SEDs are less plausible for the two SMGs, regardless of the rarity or otherwise of cold SEDs.

4.3. Benchmark Tests of the Redshift Estimates

It is informative to perform some benchmark tests using SMGs with known spectroscopic redshifts to assess whether our method returns sensible values and to evaluate systematics in our photometric redshift estimates. We have found seven bright or lensed SMGs with CO spectroscopic redshifts that have SPIRE, ~1000 μm, and radio photometry in the literature (Ivison et al. 2010; Ikarashi et al. 2011; Riechers et al. 2013; Wardlow et al. 2013; Messias et al. 2014). Figure 5 shows comparisons of their radio/(sub)mm photometric redshifts and their spectroscopic redshifts. All except HFLS3 show good agreement. The underestimation of the redshift when using the radio/(sub)mm method for HFLS3 can be explained by its abnormally high dust temperature (56 K). As the probability density distribution shows (see middle in Figure 5), there is a small local peak around the spectroscopic redshift with a T_d similar to that of HFLS3.

In addition to benchmark tests with a spectroscopic sample, we also conducted another benchmark test using 46 radio-detected ALMA-identified SMGs from ALESS with optical/near-IR photometric redshifts (Simpson et al. 2014; Swinbank et al. 2014). ALESS sources were originally 880 μm-selected SMGs and are expected to be drawn from the same population as ASXDF1100.053.1 and 231.1. We estimate radio/submm photometric redshifts using SPIRE 250–500 μm, ALMA 880 μm and VLA 1.4 GHz flux densities (see these flux densities in Table A1 of Swinbank et al. 2014). A comparison of their radio/submm-estimated photometric redshifts and optical/near-IR estimates is shown in Figure 5. We derived $\Delta z = (z_{\rm photo}^{\rm radio} - z_{\rm photo}^{\rm opt})/(1 + z_{\rm photo}^{\rm opt})$. Its median and 1$\sigma$ dispersion are −0.01 and 0.27, respectively. We should note that there is no contamination between optical/near-IR photometric redshifts of $\lesssim$4 and radio/(sub)mm photometric redshifts of $\gtrsim$5.

These benchmark tests suggest that our radio/(sub)mm photometric redshifts using multi-SEDs do not suffer strong systematics.

4.4. Cross-checking Photometric Redshifts

We first derived photometric redshifts using the average SED of 99 ALMA-identified SMGs from Swinbank et al. (2014). This redshift estimate is expected to give us the most reliable redshift for typical SMGs, but will underestimate the uncertainty due

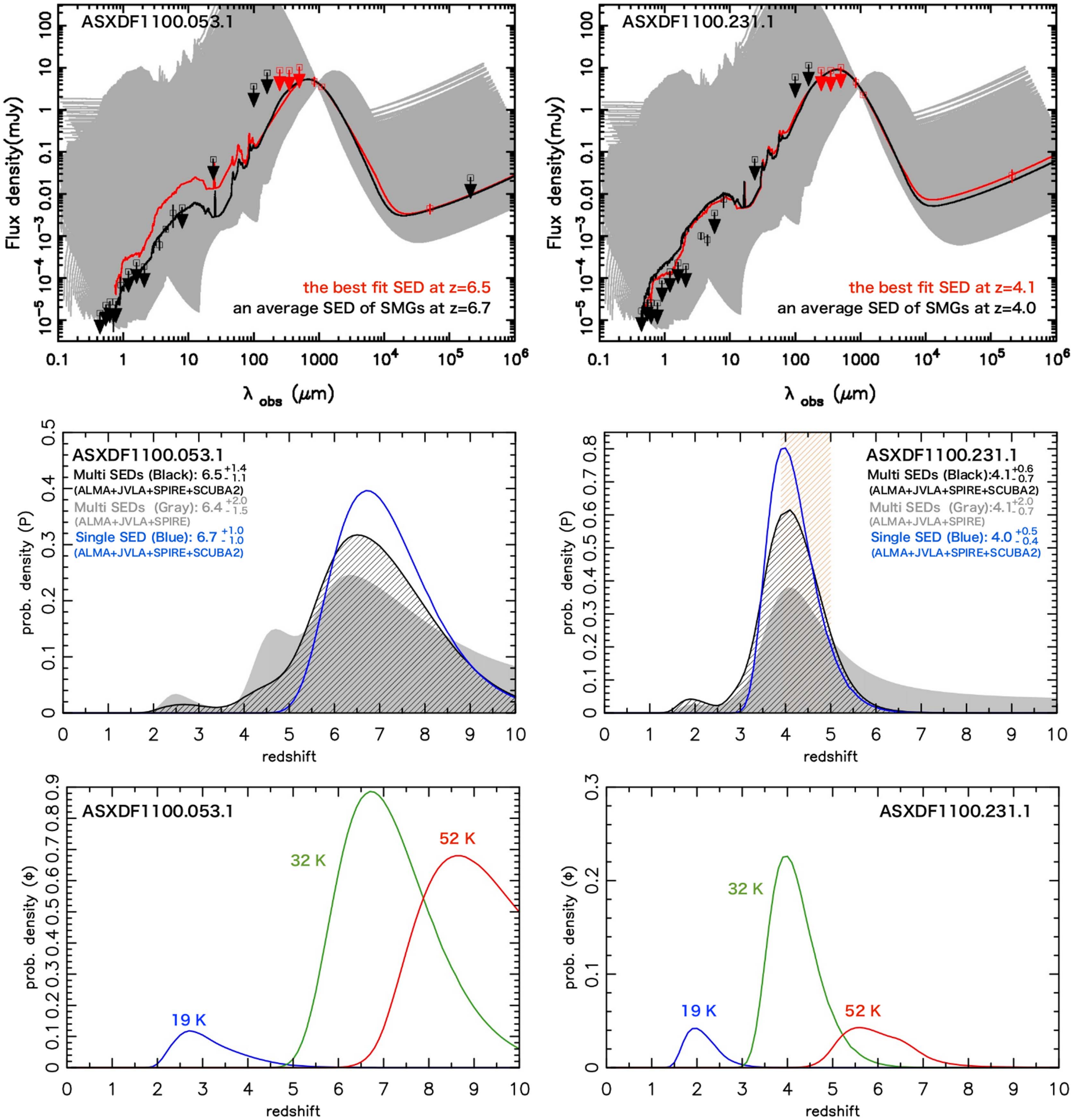

Figure 4. Radio/(sub)mm photometric redshift of ASXDF1100.053.1 and 231.1. Top: Observed photometric data and model SEDs. Red open squares mark photometric data used in our radio/(sub)mm photometric redshift estimates: JVLA 6 GHz, ALMA 1100 μm, SCUBA-2 850 μm, and upper limits in the SPIRE bands. Black open squares mark photometric data not used in our redshift estimation. The red line is the best-fit SED at the best-fit redshift in photometric redshift estimation. The gray shaded area marks a range of all fit SEDs at all redshifts. The black line represents the averaged SED of ALMA-identified SMGs at the best-fit redshift presented in Section 4.4. Middle: Redshift probability density distributions of radio/(sub)mm photometric redshift. The black hatched curve marks the redshift probability density distribution. The gray curve shows this distribution without the SCUBA-2 850 μm data. The blue line marks the distribution of a single SED template, the average SED of ALMA-identified SMGs. The derived photometric redshift for each estimate is displayed in the panels. The orange hatched area marks a redshift range where the mid-IR color of ASXDF1100.231.1 is explained by the redshifted Hα emission line in the IRAC 3.6 μm band, as discussed in Section 6. Bottom: Probability densities (Φ) for individual SEDs of 19, 32, and 52 K using all (sub)mm/radio bands that contribute different T_d temperatures to the combined photometric redshift.

to the plausible diversity of SEDs. The derived redshift probability density distributions for ASXDF1100.053.1 and 231.1, based on the average SED, show results consistent with radio/submm-based photometric redshifts (Figure 4): The respective photometric redshifts based on the average SED are $6.7^{+1.0}_{-1.0}$ and $4.0^{+0.5}_{-0.4}$.

Redshift probability densities based on our redshift estimates without SCUBA-2 850 μm data are shown in Figure 4. The 850 μm detection allows a smaller uncertainty and sharpens the redshift probability densities. This implies that the model 850 μm flux densities of the SMGs based on photometric redshifts from ALMA 1100 μm and (J)VLA radio colors and

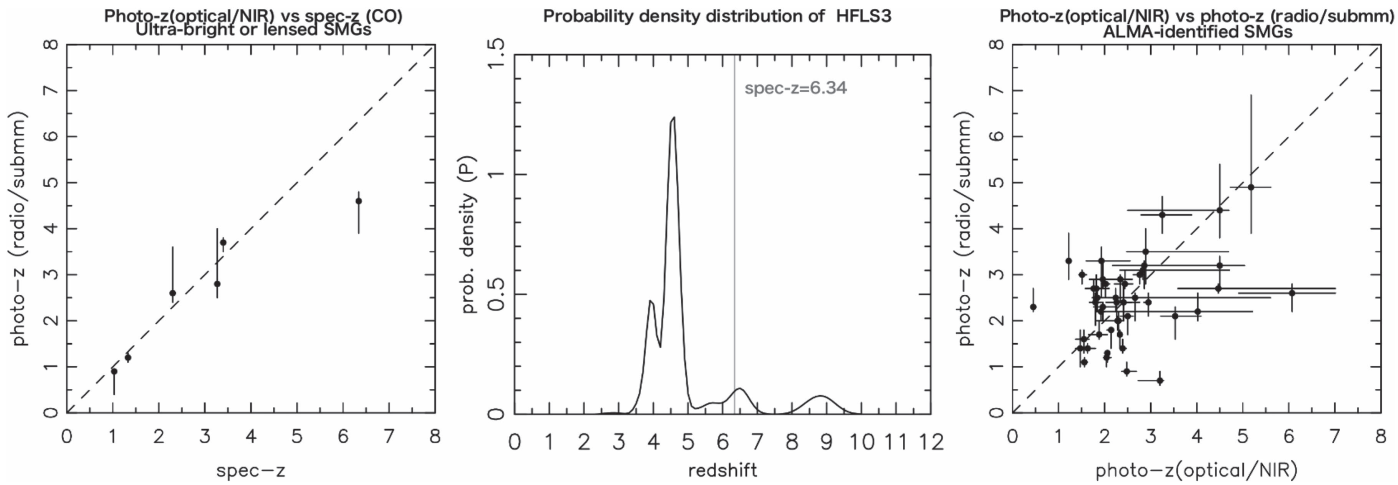

Figure 5. Radio/(sub)mm photometric redshift estimation. Left: Comparison of radio/(sub)mm photometric redshift with spectroscopic redshift obtained via CO for six bright or lensed SMGs from the literature (Ivison et al. 2010; Ikarashi et al. 2011; Riechers et al. 2013; Wardlow et al. 2013; Messias et al. 2014). Middle: Redshift probability density distribution for HFLS3, shown to explain what happens when its redshift is estimated using radio/(sub)mm photometry. Right: Comparison of radio/(sub)mm photometric redshifts with optical/near-IR photometric redshifts for 46 ALMA-identified SMGs with radio detections (Simpson et al. 2014; Swinbank et al. 2014).

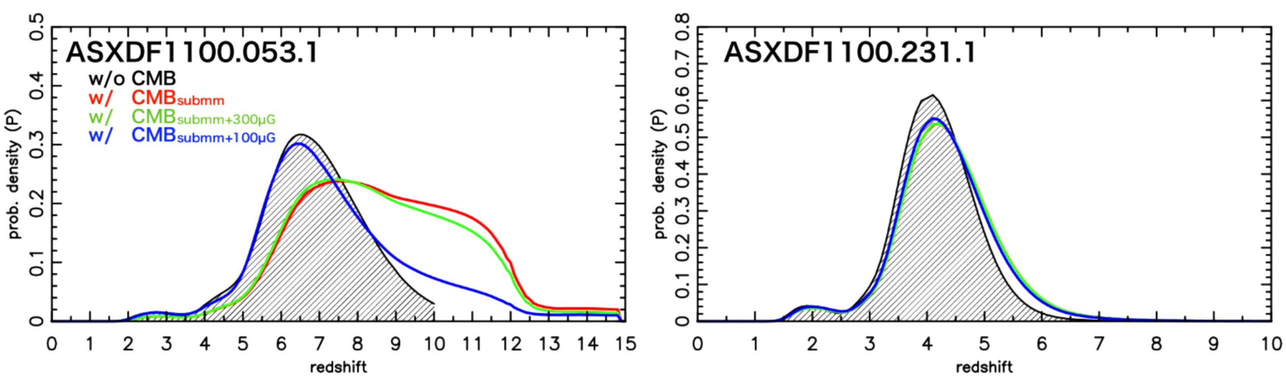

Figure 6. Redshift probability densities of radio/(sub)mm photometric redshift estimates when including the effects of the CMB for ASXDF1100.053.1 and 231.1. The gray curve is a probability density distribution without any CMB effects, i.e., it is the same plot shown in Figure 4. The red curve shows a probability density distribution with the CMB effect on observed (sub)mm flux densities. The green curve is a probability density distribution with the CMB effects on both (sub)mm and radio flux densities for $B = 300\ \mu$G. The blue curve is for $B = 100\ \mu$G. The redshift range is extended to $z = 15$ for ASXDF1100.053.1 due to the high probability of $z \geqslant 10$. For the direct comparison with the result shown in Figure 4, the probability densities are scaled in $z = 0$–10.

the upper limits at SPIRE bands are consistent with the observed 850 μm flux densities.

4.5. Possible Effects of the CMB on Redshift Estimation

In the very early Universe, the cosmic microwave background (CMB) can have effects on observed submm and radio flux densities (see, e.g., Zhang et al. 2016). Here we discuss possible contributions of the CMB to the radio/submm photometric redshifts using toy models for CMB effects.

On the basis of the predictions of CMB effects on observed total submm flux densities (da Cunha et al. 2013 deals with the effect on total flux densities, and Zhang et al. 2016 explores the spatially resolved effects), we took two CMB effects on observed submm flux densities into account: the effect on intrinsic far-IR/submm dust SEDs, and the effect on the detectability of SMGs against the CMB background. We evaluated these effects on the observed flux densities at 1100, 850, 500, 350, and 250 μm for the T_d of each SED in the same manner as da Cunha et al. (2013).

Observed radio flux densities of distant galaxies are expected to become fainter as a function of redshift because synchrotron emission is suppressed by inverse Compton (IC) losses off the CMB (Murphy 2009). The suppression of radio flux densities by the CMB depends on the strength of the magnetic field (B) in a galaxy, about which we know very little.

On the basis of observational studies of SMGs in the literature, Murphy (2009) suggested that SMGs can have a strong B, potentially $\gtrsim$300 μG. McBride et al. (2014) reported a minimum B strength of $\gtrsim$150–500 μG for local (U)LIRGs, based on observed synchrotron flux densities. They expected a stronger B, >600 μG, based on measurements of Zeeman splitting in OH masers. Given that ASXDF1100.053.1 and 231.1 have compact mm-wave sizes and surface IR luminosity densities similar to those of local ULIRGs (see Sections 5 and 6.2), these studies also support a strong B for our sample.

In this paper, we investigate how the effect of the CMB on radio emission contributes to radio/mm photometric redshift estimates where $B = 100$ and 300 μG: 300 μG is taken as the value for SMGs, and 100 μG is used to examine what happens when the magnetic field is weaker. We determined the predicted suppression of nonthermal emission by the CMB using the equations and assumptions provided in Murphy (2009): we modeled the synchrotron emission by subtracting

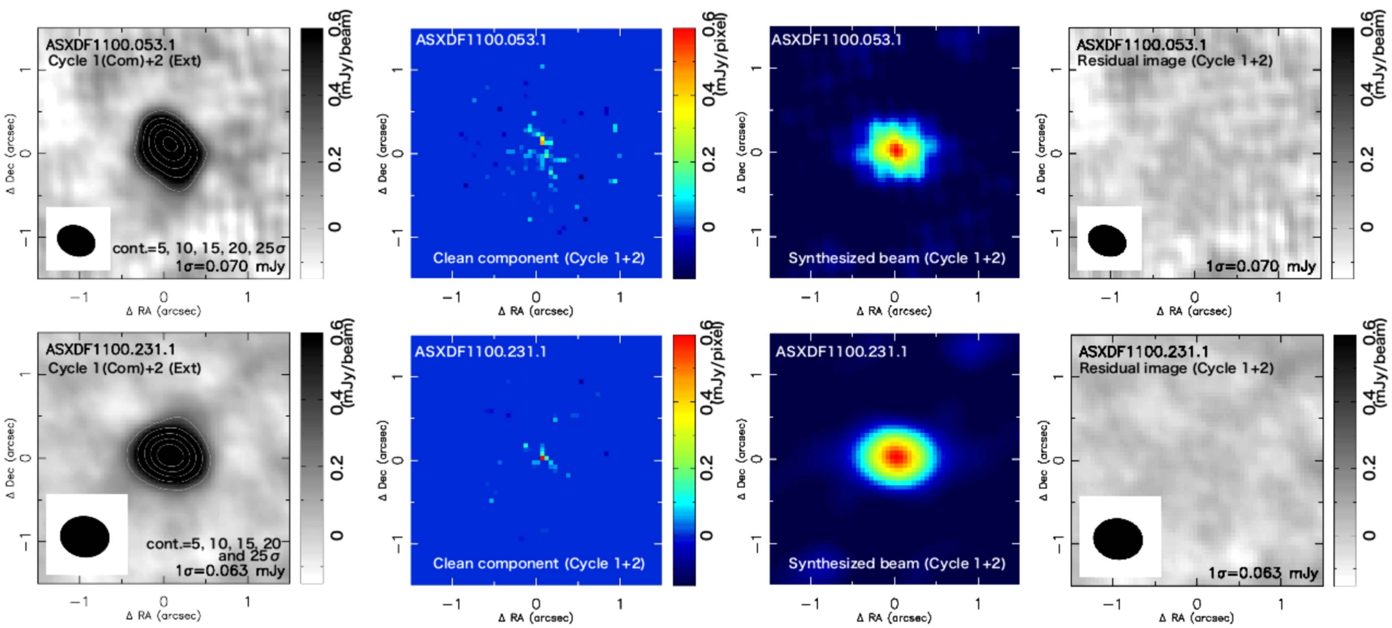

Figure 7. ALMA images of ASXDF1100.053.1 and 231.1. First column: Cleaned ALMA 1100 μm continuum images taken in ALMA Cycles 1 and 2. Synthesized beams of the combined data are $0\farcs46 \times 0\farcs35$ (PA, 69°) and $0\farcs57 \times 0\farcs48$ (PA, 82°) for ASXDF1100.053.1 and 231.1, respectively. Contours are shown at 5, 10, 15, 20, and 25σ. The flux density unit is mJy beam^{-1}. The rms noise level is shown at the bottom in each panel. Second column: Clean component maps of the combined ALMA images are shown in the middle panel. The clean component maps were obtained by cleaning down to 1σ. Third column: Synthesized beams for the combined ALMA images. Fourth column: Residual maps after subtracting the clean components convolved with the synthesized beams. The pixel scale is $0\farcs05$ in all images.

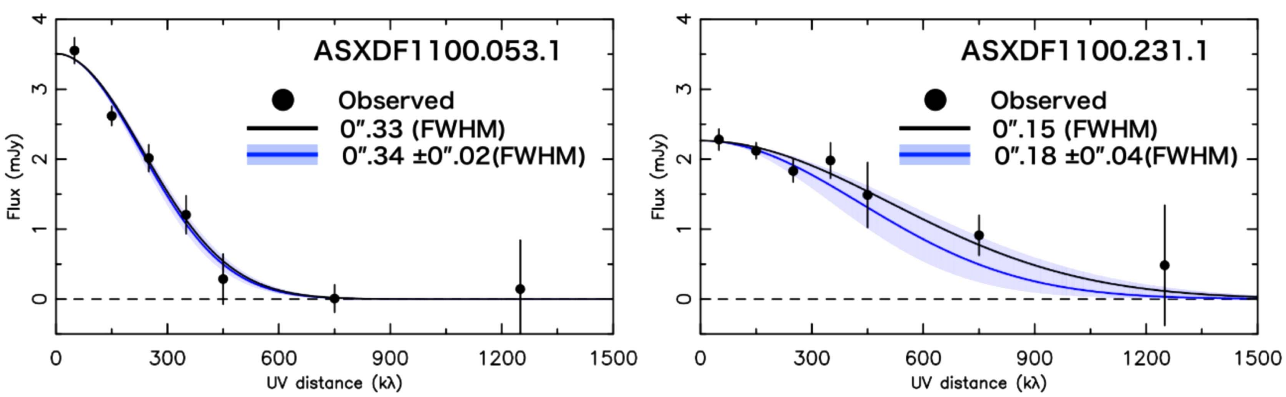

Figure 8. ALMA *uv*-distance vs. amplitude plots of ASXDF1100.053.1 and 231.1. Black solid points are the observed data. Binning sizes in *uv* distance are 100 kλ out to 500 kλ and 500 kλ between 500 and 1500 kλ. The black line is a *uv*-amp model of the best-fit Gaussian component. The blue line and shaded area are possible solutions for the corrected source size, with errors based on Monte Carlo simulations.

free–free and dust emission, where we model free–free emission from $L_{\rm IR}$ based on the Equation (16) in the literature.

Figure 6 shows the resulting redshift probability density distribution, including the CMB effects, for both ASXDF1100.053.1 and 231.1: (1) probability density without any CMB effects; (2) with the CMB effect at (sub)mm wavelengths; (3) with both of the CMB effects ($B = 300\ \mu$G); and (4) with both of the CMB effects ($B = 100\ \mu$G). We see that taking the effects of the CMB into account pushes the photometric redshifts to higher values. However, as we do not have spectroscopic redshifts for the two SMGs, we cannot determine how strong this effect really is.

5. ALMA Millimeter-wave Source Sizes

The first millimetric size measurements of ASXDF1100.053.1 and 231.1 were determined using our ALMA Cycle-1 data, which covered up to a *uv* distance of $\sim$400 kλ, with a synthesized beam size of $\sim0\farcs70$ (FWHM— Ikarashi et al. 2015). These visibility data assumed Gaussian profiles and suggested compact millimetric sizes: $0.28^{+0.04}_{-0.04}$ and $0.12^{+0.08}_{-0.08}$ arcsec (FWHM) for ASXDF1100.053.1 and 231.1, respectively. In this section, we reassess their millimetric sizes by combining Cycle-1 and -2 data, which now cover up to 1500 kλ.

In Figure 7 we show ALMA maps for ASXDF11100.053.1 and 231.1. These maps were generated from the combined ALMA 1100 μm data, cleaning down to the 1σ depth in a circle with a radius of 1 arcsecond using the CLEAN task in CASA. The pixel scale is $0\farcs05$ pixel^{-1}.

5.1. Millimeter-wave Size Measurements in Visibility Data

First, we measure mm-wave sizes of ASXDF1100.053.1 and 231.1 with the ALMA visibility data in the same manner as Ikarashi et al. (2015). We use *uv*-distance versus amplitude plots (hereafter *uv*-amp plots) for the measurements (Figure 8).

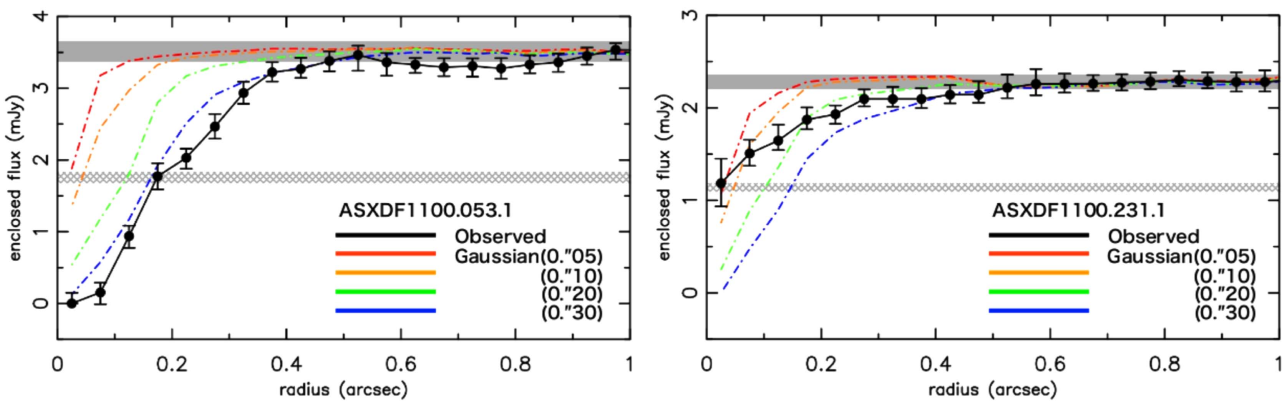

Figure 9. Enclosed flux densities as a function of radius measured in the clean component maps for ASXDF1100.053.1 and 231.1. The black solid line shows observed data. Colored dot–dashed lines show enclosed flux densities of models with Gaussian profiles with various sizes from 0.″05 to 0.″30 (FWHM). The enclosed flux density profiles of Gaussian models are reproduced in the same manner using the actual data, and are taken from simulations presented in the Appendix. Filled gray lines show total ALMA flux densities with errors measured independently in the beam-convolved ALMA images that are listed in Table 1. Hatched gray lines show half of the total ALMA flux densities with the errors for finding half-light radii.

Modeling sources with *uv*-amp plots helps us to avoid underestimating their flux densities, since we can interpolate/extrapolate across incomplete visibility coverage. We assume symmetric Gaussian profiles, as is usually done in the literature. Circularized effective radii estimated using *uv* plots are useful, even for sources with asymmetric profiles (Ikarashi et al. 2015). Bin sizes adopted in *uv* distance are 100 kλ out to 500 kλ and 500 kλ between 500 and 1500 kλ. The estimated sizes of ASXDF1100.053.1 and 231.1 are then 0.″33 and 0.″15 (FWHM), respectively (Figure 8). Correcting these "raw" mm-wave sizes for systematic effects using Monte Carlo simulations, the mm-wave sizes are then $0.''34^{+0.02}_{-0.02}$ and $0.''18^{+0.04}_{-0.04}$ for ASXDF1100.053.1 and 231.1, respectively, consistent with our previous measurements.

5.2. Millimeter-wave Size Measurements in Clean Component Maps

Next, we derive $R_{c,e}$ for ASXDF1100.053.1 and 231.1 using ALMA clean component maps, as shown in Figure 7. These maps were generated from the combined ALMA 1100 μm data by running the CLEAN task in CASA. Our motivation is to measure $R_{c,e}$ directly, without any assumed model, exploiting the high signal-to-noise ratios of $\sim$30.

Figure 9 shows enclosed flux densities as a function of radius for ASXDF1100.053.1 and 231.1, measured in the clean component maps. Total flux densities of the two SMGs in the clean component maps are consistent with the fluxes measured in the beam-convolved ALMA continuum images listed in Table 2, despite the potential absence of any $<1\sigma$ components. Flux density errors are estimated based on Monte Carlo simulations using 100 independent sets of visibility data generated from the actual ALMA data. In the simulations, we input a Gaussian model with the same flux as one of the real sources, then imaged these data, generating clean component maps. We then measured the enclosed flux densities in the same manner as that for the real sources. We repeated this process with source sizes between 0.″025 and 0.″800 in steps of 0.″025 (FWHM) to reconstruct observed enclosed flux densities in each bin. We adopted a flux density error in the simulation with an enclosed flux density closest to a real measured flux density in each radius bin as the error for the real measurements. We refer to the Appendix, where we describe the simulations in more detail.

For ASXDF1100.053.1, based on the obtained enclosed flux density plot and the total flux density, we determine $R_{c,e}$ of $0.17^{+0.02}_{-0.01}$ arcsec. Since the half-width at half-maximum of a symmetric Gaussian is equivalent to $R_{c,e}$, the size obtained from the clean component map is consistent with that from the *uv*-amp plot.

For ASXDF1100.231.1, the flux density in the center pixel is $1.19^{+0.27}_{-0.24}$ mJy beam^{-1}. This corresponds to 52^{+7}_{-6}% of its total flux density. From the obtained enclosed flux density plot, with linear interpolation, we find $R_{c,e} = 0.025^{+0.015}_{-0.00}$ arcsec, meaning the half-light radius of ASXDF1100.231.1 is $\leqslant 0.''04$. $R_{c,e}$ determined via the clean component map is approximately twice smaller than the half-light radius determined from the *uv*-amp plot, $R_{c,e} = 0.09$ arcsec.

The enclosed flux density plot suggests that ASXDF1100.231.1 cannot be modeled with a single Gaussian profile: ASXDF1100.231.1 appears to comprise a compact intense mm-emitting region, located in its center region, and a fainter extended region. The different $R_{c,e}$ values determined using the *uv*-amp plot and the clean component map can thereby be understood.

Monte Carlo simulations of source size measurements in ALMA clean component maps are described in the Appendix. According to these simulations, this method of measuring source sizes is useful down to $R_{c,e} = 0.''025$. The simulations show that the measured sizes of ASXDF1100.053.1 and 231.1 are not expected to suffer large systematic errors.

6. On the Nature of ASXDF1100.053.1 and 231.1

Here we determine the properties of ASXDF1100.053.1 and 231.1 from multiwavelength data, adopting the radio/submm photometric redshifts. We discuss the possible role of the two SMGs, which are faint in the *Herschel* bands and at optical/near-/mid-IR and radio wavelengths, in the context of galaxy evolution.

6.1. Optical/Near-IR SED Fitting

In order to characterize the optical/near-IR properties of ASXDF1100.053.1 and 231.1, we conducted an SED-fitting analysis across optical–mid-IR wavelengths. We adopted a

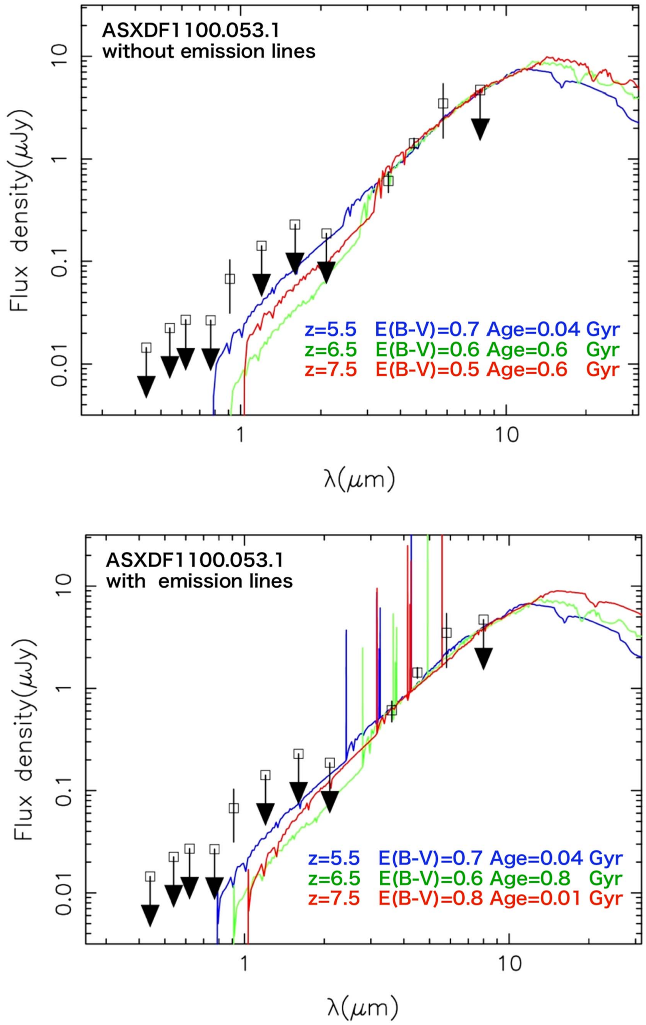

Figure 10. ASXDF1100.053.1 SED at observed optical/near-/mid-IR wavelengths. Top: Best-fit SEDs, ignoring emission lines, for $z = 5.5$, 6.5 and 7.5, as obtained with *Le Phare*. Black points correspond to the observed flux densities, while arrows indicate 2σ upper limits. Bottom: Best-fit SEDs, this time including emission lines.

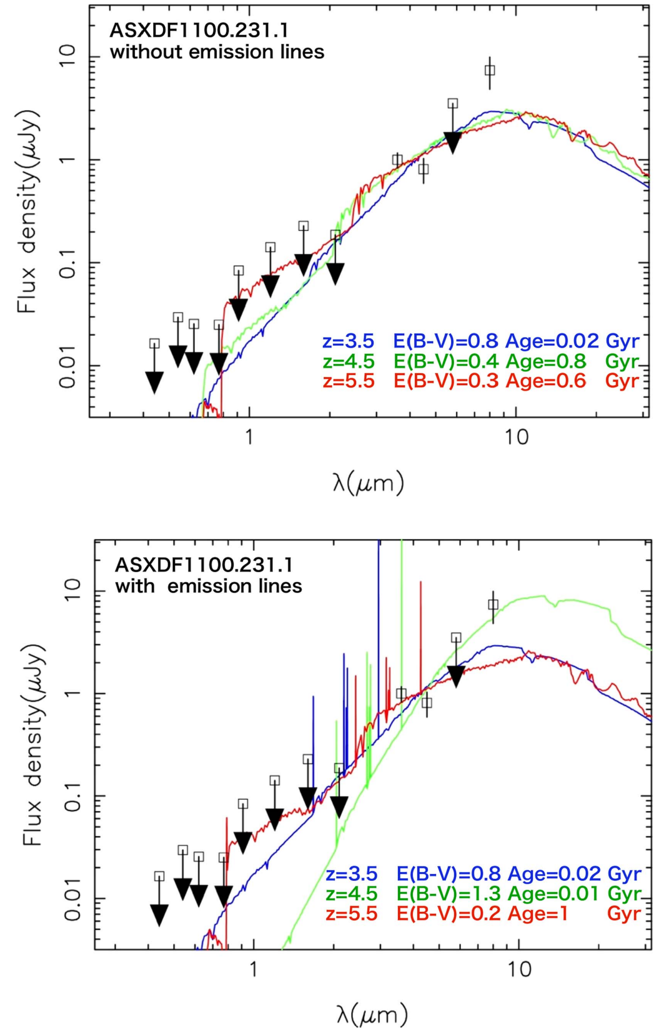

Figure 11. ASXDF1100.231.1 SED at observed optical/near-/mid-IR wavelengths. Top: Best-fit SEDs, without emission lines, toward ASXDF1100.231.1 for $z = 3.5$, 4.5 and 5.5, as obtained with *Le Phare*. Black points correspond to the observed flux densities, while arrows indicate 2σ upper limits. Bottom: Best-fit SEDs, this time including emission lines.

Chabrier IMF (Chabrier 2003) and stellar population synthesis models by Bruzual & Charlot (2003). Dust extinction was considered according to the prescription by Calzetti et al. (2000). We adopted a metallicity of $Z_{\odot} = 0.02$. We performed the analysis using the code *Le Phare* (Arnouts et al. 1999; Ilbert et al. 2006). These SMGs are detected in only three or four filters in the available optical/mid-IR broadband images, similar to the extremely red mm source analyzed by Caputi et al. (2014). We derived optical/near-IR properties at fixed redshifts of $z = 5.5$, 6.5 and 7.5 for ASXDF1100.053.1, and $z = 3.5$, 4.5, and 5.5 for ASXDF1100.231.1 to reduce parameter space. These values span a range of approximately ±1 around the best radio/submm photometric redshifts. We conducted the SED fitting both with and without considering emission lines. Free parameters were star formation history, age, and dust extinction.

The best-fit SEDs are shown in Figures 10 and 11 and the derived parameters are summarized in Table 3. The observed optical/mid-IR SED of ASXDF1100.053.1 is well fit at $z = 5.5$, 6.5, and 7.5, both with and without emission lines, as the minimum χ^2s show. ASXDF1100.053.1 has an extremely red color, $[3.6] - [4.5] = 0.9$, which can be reproduced by heavy dust extinction, $E(B - V) \sim 0.6$–0.8. In all cases, the observed z'-band flux is not reproduced, but the detection at z' band is only marginal (2σ). If the detection is real, the rest-frame UV light may come from less obscured regions in ASXDF1100.053.1. It is worth mentioning that the Lyα line should fall in the z' band at $z = 6.0$–7.2, but the importance of this line in emission at such redshifts is still unclear.

The observed optical/mid-IR SED of ASXDF1100.231.1 is not well fit by the model SEDs. Its unusual colors, $[2.2] - [4.5] < 1.7$, $[3.6] - [4.5] = -0.1$, and $[4.5] - [8.0] = 2.3$, imply a possible excess in the IRAC 3.6 μm band. Remarkably, the SED of ASXDF1100.231.1 is best fit by the model at $z = 4.5$, including emission lines, with the heaviest extinction of our SED fits. The Hα emission line enters the IRAC 3.6 μm band at $z = 3.9$–5.0, consistent with the radio/submm photometric redshift, $4.1^{+0.6}_{-0.7}$ (Figure 4). Interestingly, 2 of 77 ALMA-identified SMGs in Simpson et al. (2014), ALESS1.2 and 65.1, have a similar color and excesses in the 3.6 μm band ($[3.6] - [4.5] < 0$, $[2.2] - [4.5] > 0$, and $[4.5] - [8.0] > 0$), and have $z_{\rm photo-z,opt} = 4.65^{+2.34}_{-1.02}$ (Simpson et al. 2014) and $z_{\rm spec} = 4.4445 \pm 0.0005$ (Swinbank et al. 2012), respectively.

Table 3
Derived Properties of ASXDF1100.053.1 and 231.1

	Stellar Mass	$\chi^2_{\rm best}$	$L_{\rm IR}$(8–1000 μm)		SFR(IR)		$R_{\rm c,e}$	$\Sigma_{L{\rm IR}}$
	($M_\odot$)		without CMB (10^{12} $L_\odot$)	with CMB (10^{12} $L_\odot$)	without CMB ($M_\odot$ yr^{-1})	with CMB ($M_\odot$ yr^{-1})	(kpc)	($L_\odot$ kpc^{-1})
ASXDF1100.053.1 without emission lines								
$z = 5.5$	$1.2^{+2.5}_{-0.81} \times 10^{11}$	3.4	5.8 ± 0.25	6.5 ± 0.28	580 ± 25	650 ± 28	$1.05^{+0.06}_{-0.03}$	$1.0^{+0.05}_{-0.07} \times 10^{12}$
$z = 6.5$	$1.0^{+4.8}_{-0.90} \times 10^{11}$	4.5	5.8 ± 0.25	6.8 ± 0.29	580 ± 25	680 ± 29	$0.95^{+0.05}_{-0.03}$	$1.2^{+0.06}_{-0.07} \times 10^{12}$
$z = 7.5$	$1.6^{+10}_{-1.4} \times 10^{11}$	4.4	6.0 ± 0.26	7.4 ± 0.32	600 ± 26	740 ± 32	$0.88^{+0.05}_{-0.03}$	$1.5^{+0.08}_{-0.09} \times 10^{12}$
ASXDF1100.053.1 with emission lines								
$z = 5.5$	$1.0^{+2.4}_{-0.69} \times 10^{11}$	2.8	5.8 ± 0.25	6.5 ± 0.28	580 ± 25	650 ± 28	$1.05^{+0.06}_{-0.03}$	$1.0^{+0.05}_{-0.07} \times 10^{12}$
$z = 6.5$	$8.6^{+42}_{-7.3} \times 10^{10}$	4.2	5.8 ± 0.25	6.8 ± 0.29	580 ± 25	680 ± 29	$0.95^{+0.05}_{-0.03}$	$1.2^{+0.06}_{-0.07} \times 10^{12}$
$z = 7.5$	$1.7^{+11}_{-1.6} \times 10^{11}$	3.8	6.0 ± 0.26	7.4 ± 0.32	600 ± 26	740 ± 32	$0.88^{+0.05}_{-0.03}$	$1.5^{+0.08}_{-0.09} \times 10^{12}$
ASXDF1100.231.1 without emission lines								
$z = 3.5$	$4.5^{+8.1}_{-3.9} \times 10^{9}$	12	4.3 ± 0.15	4.5 ± 0.16	430 ± 15	450 ± 16	$\leqslant 0.25$	$\geqslant 1.5 \times 10^{13}$
$z = 4.5$	$2.6^{+3.1}_{-1.5} \times 10^{10}$	10	3.9 ± 0.14	4.2 ± 0.15	390 ± 14	420 ± 15	$\leqslant 0.22$	$\geqslant 1.7 \times 10^{13}$
$z = 5.5$	$3.3^{+3.6}_{-1.9} \times 10^{10}$	7.5	3.8 ± 0.13	4.2 ± 0.15	380 ± 13	420 ± 15	$\leqslant 0.20$	$\geqslant 2.1 \times 10^{13}$
ASXDF1100.231 with emission lines								
$z = 3.5$	$4.3^{+7.8}_{-3.7} \times 10^{9}$	12	4.3 ± 0.15	4.5 ± 0.16	430 ± 15	450 ± 16	$\leqslant 0.25$	$\geqslant 1.5 \times 10^{13}$
$z = 4.5$	$2.6^{+2.3}_{-1.2} \times 10^{10}$	5.5	3.9 ± 0.14	4.2 ± 0.15	390 ± 14	420 ± 15	$\leqslant 0.22$	$\geqslant 1.7 \times 10^{13}$
$z = 5.5$	$2.8^{+3.3}_{-1.6} \times 10^{10}$	8.4	3.8 ± 0.13	4.2 ± 0.15	380 ± 13	420 ± 15	$\leqslant 0.20$	$\geqslant 2.1 \times 10^{13}$

The stellar mass of ASXDF1100.053.1 derived from the SED fitting without emission lines would be [1.0–1.6] $\times$ 10^{11} $M_\odot$ at $z = 5.5$–7.5. When the emission lines are taken into account, the stellar mass becomes [0.8–1.7] $\times$ 10^{11} $M_\odot$. For ASXDF1100.231.1: ignoring emission lines yields [0.5–3.3] $\times$ 10^{10} $M_\odot$ at $z = 3.5$–5.5; with emission lines, the value is [0.4–2.8] $\times$ 10^{10} $M_\odot$. These stellar masses, which are summarized in Table 3, are consistent with the masses of known ALMA-identified SMGs (e.g., da Cunha et al. 2015).

6.2. Millimeter Properties

The IR luminosities ($L_{\rm IR}$, rest-frame 8–1000 μm) and star formation rates (SFRs) of ASXDF1100.053.1 and 231.1 can be estimated from the ALMA 1100 μm continuum, for which we adopted the average SED of ALMA-identified SMGs from Swinbank et al. (2014), using

$$\mathrm{SFR}(M_\odot\ \mathrm{yr}^{-1}) = 1.0 \times 10^{-10} L_{\rm IR}(L_\odot) \quad (4)$$

for a Chabrier IMF (Chabrier 2003), according to the formula provided by Kennicutt (1998).

For ASXDF1100.053.1, $L_{\rm IR} = [4.8 - 6.0] \times 10^{12}\,L_\odot$ at $z = 5.5$–7.5, and the SFR is in the range 580–600 $M_\odot$ yr^{-1}. These $L_{\rm IR}$ and SFR estimates are largely independent of redshift because of the strong negative K correction at submm wavelengths (e.g., Blain et al. 2002). When we consider the CMB effects on the observed 1100 μm fluxes, we find $L_{\rm IR} = [6.5$–$7.4] \times 10^{12}\,L_\odot$ and an SFR between 650–740 $M_\odot$ yr^{-1}.

The corresponding values for ASXDF1100.231.1 without the CMB correction are $L_{\rm IR} = [3.8 - 4.3] \times 10^{12}\,L_\odot$ at $z =$ 3.5–5.5, with an SFR in the range 380–430 $M_\odot$ yr^{-1}; with CMB corrections: $L_{\rm IR} = [4.2$–$4.5] \times 10^{12}\,L_\odot$ and 420–450 $M_\odot$ yr^{-1}. These values and errors are listed in Table 3.

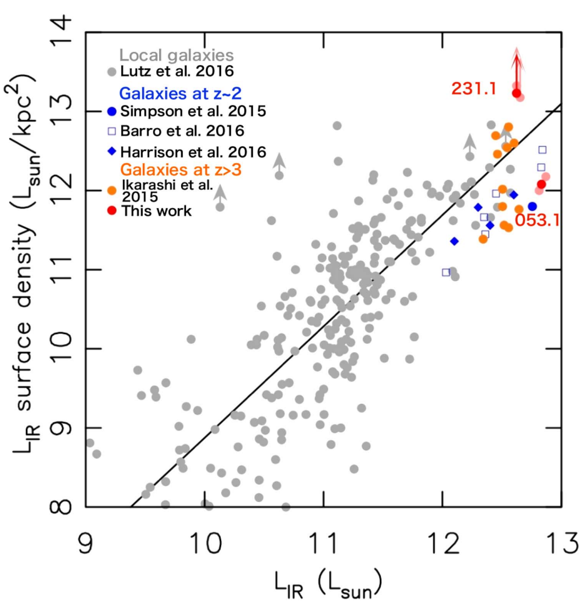

Figure 12. IR luminosity vs. surface IR luminosity density plots for known local and high-redshift galaxies. Red dots mark ASXDF1100.053.1 at $z = 6.5$ and 231.1 at $z = 5.5$. Pink dots mark ASXDF1100.053.1 at $z = 5.5$ and 7.5, and 231.1 at $z = 3.5$ and 5.5, to show uncertainties due to redshift. Gray dots mark local galaxies, and the black solid line shows the fit line for local galaxies presented by Lutz et al. (2016). Blue markers show known $z \sim 2$ galaxies: open squares mark so-called main-sequence galaxies (Barro et al. 2016), filled diamonds represent X-ray AGNs (Harrison et al. 2016), and the filled circle marks the median for SMGs (Simpson et al. 2015a). Orange dots mark $z \gtrsim 3$ candidate SMGs by Ikarashi et al. (2015). The sizes of these high-redshift galaxies in the literature come from measurements using ALMA data. $L_{\rm FIR}$ (40–120 μm) was converted into $L_{\rm IR}$ (rest-frame 8–1000 μm) based on an expected offset of 0.3 in log scale, based on the empirical far-IR/radio luminosity correlation (Yun et al. 2001) and the IR/radio luminosity correlation (Bell 2003).

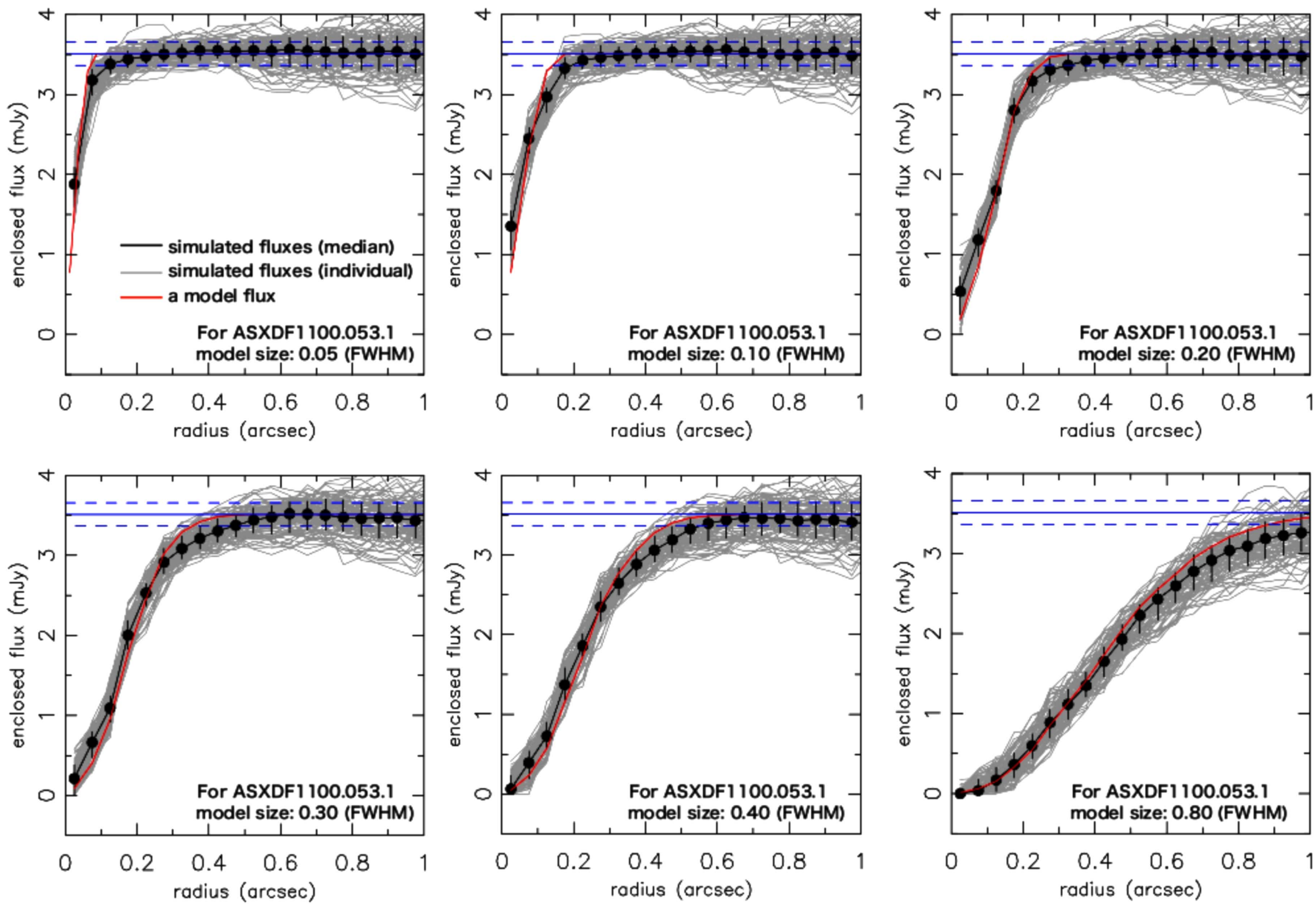

Figure 13. Simulated enclosed fluxes using symmetric Gaussian models as a function of radius for ALMA data of ASXDF1100.053.1. Black dots and vertical lines mark medians and 1σ dispersions of the 100 simulated fluxes. Gray lines show enclosed fluxes of the 100 mock sources. The red line marks a raw flux of an input Gaussian model with a spatial sampling of 0$''$.05 pixel^{-1} (for a model size of 0$''$.05, a sampling of 0$''$.025 pixel^{-1}). Blue solid and dashed lines mark the total flux and error of ASXDF1100.053.1 independently measured in the ALMA beam-convolved image. Here we plot model sizes of 0$''$.05, 0$''$.10, 0$''$.20, 0$''$.30, 0$''$.40, and 0$''$.80 (FWHM) as representatives of all simulated sizes.

As was revealed in Section 5, ASXDF1100.053.1 and 231.1 have compact mm-wave sizes. From the clean component maps, we find $R_{\rm c,e} = 0.17^{+0.02}_{-0.01}$ arcsec for ASXDF1100.053.1, and $\leqslant$0.04 arcsec for ASXDF1100.231.1. Given physical scales at $z = 5.5$–7.5, the $R_{\rm c,e}$ of ASXDF1100.053.1 corresponds to 0.88–1.1 kpc. Given the physical scales at $z = 3.5$–5.5, the measured $R_{\rm c,e}$ for ASXDF1100.231.1 is $\leqslant$0.20–0.25 kpc. For further characterization of sizes, we also derived $R_{\rm c,0.9}$, the circularized radii that include 90% of the total flux density from the enclosed flux functions (Figure 9): $R_{\rm c,0.9}$ (median) of ASXDF1100.053.1 for $z = 5.5$–7.5 is 2.2–2.6 kpc and that of ASXDF1100.231.1 for $z = 3.5$–5.5 is 1.6–2.1 kpc. We applied systematic corrections based on the simulations shown in the Appendix. The compact nature of ASXDF1100.231.1 is similar to the few $\times$100 pc clumps discovered through 0$''$.015–0$''$.05 imaging of SMGs by Iono et al. (2016) and Oteo et al. (2016). These $R_{\rm c,0.9}$ values are consistent with suggestions of extended emission in SMGs in Hodge et al. (2016) and Iono et al. (2016).

The surface IR luminosity densities ($\Sigma_{L_{\rm IR}}$) based on $R_{\rm c,e}$ and $L_{\rm IR}$ are $[1.0 - 1.5] \times 10^{12}\,L_{\odot}\,{\rm kpc}^{-2}$ at $z = 5.5$–7.5 for ASXDF1100.053.1. The respective densities of ASXDF1100.231.1 are $[1.5$–$2.1] \times 10^{13}\,L_{\odot}$ kpc^{-2} for $z = 3.5$–5.5. Figure 12 shows $L_{\rm IR}$ versus surface IR luminosity density for ASXDF1100.053.1 and 231.1 and demonstrates that for $z \gtrsim 4$ they are similar to local and high-redshift galaxies from Ikarashi et al. (2015), Simpson et al. (2015a), Barro et al. (2016), Harrison et al. (2016), and Lutz et al. (2016). For $z \gtrsim 6$ and $z \sim 4$, respectively, ASXDF1100.053.1 and 231.1 have surface IR luminosity densities consistent with an empirical $L_{\rm IR} - \Sigma_{L_{\rm IR}}$ relation $(\log(\Sigma_{\rm FIR}) = 8.997 + 1.408 \times (\log(L_{\rm IR}) - 10))$ derived for local galaxies in Lutz et al. (2016). The derived physical sizes and surface IR luminosities are summarized in Table 3.

6.3. Progenitors of $z \gtrsim 3$ Compact Quiescent Galaxies?

Based on their mm-wave sizes and redshift estimates, Ikarashi et al. (2015) suggested that ASXDF1100.053.1 and 231.1 may be the progenitors of $z \sim 2$ compact quiescent galaxies (cQGs), the evolutionary scenario suggested by Toft et al. (2014). cQGs have now been reported out to $z \sim 4$ (Straatman et al. 2015). Their stellar components have $R_{\rm c,e} = 0.3$–3.2 kpc, with the median of 0.63 ± 0.18 kpc. ASXDF1100.053.1 and 231.1 have compact enough starburst regions to evolve into cQGs at $z \sim 3$–4. ASXDF1100.053.1 has already created a stellar mass comparable to that found in cQGs at $z \sim 2$, $[0.4$–$5] \times 10^{11}\,M_{\odot}$ (e.g., Belli

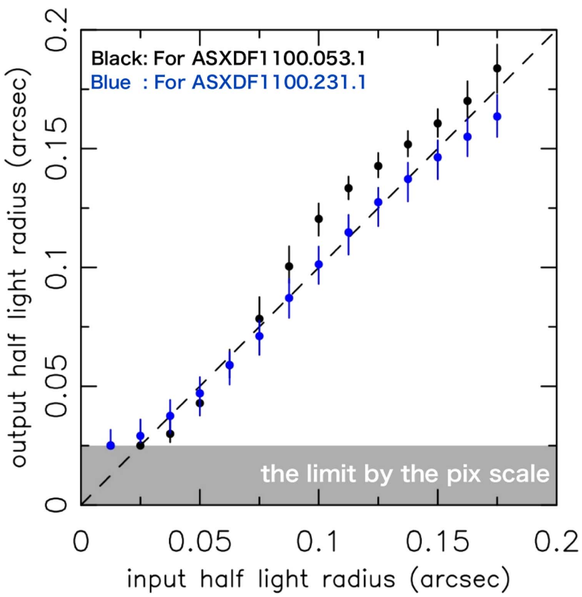

Figure 14. Comparisons of input and output half-light radii derived from Monte Carlo simulations using symmetric Gaussian models. These simulations used the noise visibility data that were generated from the actual ALMA data for ASXDF1100.053.1 (black) and 231.1 (blue). Output size and measured half-light radii were obtained in the same manner as real measurements. The gray shaded region marks the limit for output sizes for a pixel scale of 0$''$.05 pixel^{-1}.

et al. 2014; Krogager et al. 2014) and at $z \sim 3$–4, [0.4–1.8] $\times$ 10^{11} $M_\odot$ (Straatman et al. 2015), based on a Chabrier IMF (Chabrier 2003). Furthermore, given the SMG duty cycle of $t_{\rm burst} = 42^{+40}_{-29}$ Myr suggested in Toft et al. (2014), and the derived SFRs by mm measurements, its stellar mass is expected to increase by $\approx$[0.8–6] $\times$ 10^{10} $M_\odot$.

The observed stellar mass of ASXDF1100.231.1 is small in comparison with known cQGs, although there are large uncertainties. ASXDF1100.231.1 will generate an additional $\approx$[0.5–4] $\times$ 10^{10} $M_\odot$ of stars via its ongoing star formation, and can thus become similarly massive to the known cQGs.

From these facts, it seems clear that ASXDF1100.053.1 and 231.1 can potentially evolve into cQGs at $z \gtrsim 3$, although it depends on their remaining gas masses and whether they quench their star formations on short timescales, i.e., the $t_{\rm burst}$ noted above.

7. Summary

We have conducted a detailed multiwavelength study of two ALMA-identified SMGs, ASXDF1100.053.1 and 231.1, which have extremely red submm colors, aiming to constrain their redshifts and better understand their nature. Based on their radio/submm colors, we determined redshifts of $6.5^{+1.4}_{-1.1}$ and $4.1^{+0.6}_{-0.7}$ for ASXDF1100.053.1 and 231.1, respectively. We quantified the influence of the CMB on these photometric redshifts using simple models, finding that even at $z \gtrsim 6$, the effects of the CMB do not lead to significant overestimation.

We measured mm-wave sizes of ASXDF1100.053.1 and 231.1 in deep ALMA continuum images. The derived circularized half-light radii of ASXDF1100.053.1 and 231.1 are $\sim$1 and $\lesssim$0.2 kpc, respectively. Their surface IR luminosity densities are $\sim 1 \times 10^{12}$ and $\gtrsim 1.5 \times 10^{13}$ $L_\odot$ kpc^{-2}, comparable to those of local (U)LIRGs and consistent with a known empirical trend in $L_{\rm IR} - \Sigma_{L_{\rm IR}}$ seen for local galaxies.

From an optical/near-/mid-IR SED analysis of ASXDF1100.053.1 and 231.1, adopting their radio/submm photometric redshifts, we found that ASXDF1100.231.1 has near-/mid-IR colors consistent with the existence of a redshifted Hα line at $z = 4$–5 in the IRAC 3.6 μm band. The derived stellar masses of ASXDF1100.053.1 and 231.1 are comparable to those of known SMGs.

Given the observed stellar masses, SFRs, and typical cycle times of SMGs, we found that ASXDF1100.053.1 and 231.1 can evolve into cQGs at $z \gtrsim 3$. Our intensive studies of SMGs at $z \gtrsim 4$, using the new capabilities of ALMA and JVLA, have allowed us to discover plausible candidate $z \gtrsim 6$ and $z \sim 4$ SMGs that are too heavily dust-obscured to be detected in even the deepest optical/near-/mid-IR images.

This paper makes use of the following ALMA data: ADS/JAO.ALMA#2012.1.00326.S. and 2013.1.00781.S. ALMA is a partnership of ESO (representing its member states), NSF (USA) and NINS (Japan), together with NRC (Canada) and NSC and ASIAA (Taiwan), in cooperation with the Republic of Chile. The Joint ALMA Observatory is operated by ESO, AUI/NRAO, and NAOJ. The National Radio Astronomy Observatory is a facility of the National Science Foundation operated under cooperative agreement by Associated Universities, Inc. S.I. and K.I.C. acknowledge the support of the Netherlands Organization for Scientific Research (NWO) through the Top Grant Project 614.001.403. S.I. was supported by the ALMA Japan Research Grant of NAOJ Chile Observatory, NAOJ-ALMA-0036, 60, 96, and 132. This work was supported by Grant-in-Aid for JSPS Fellows Number 25-10420. R.J.I. acknowledges support from ERC in the form of the Advanced Grant, 321302, COSMICISM. Y.T. is supported by JSPS KAKENHI (No. 15H02073). C.L. is funded by a Discovery Early Career Researcher Award (DE150100618). Parts of this research were conducted by the Australian Research Council Centre of Excellence for All-sky Astrophysics (CAASTRO), through project number CE110001020. H.U. is supported by JSPS Grant-in-Aid for Research Activity Start-up (16H06713). I.A. acknowledges the support of Mexican CONACyT research grants CB-2011-01-167291.

Facilities: ALMA, VLA, ASTE, *Herschel*, *Spitzer*, UKIRT, Subaru.

Appendix
Simulations of Enclosed Fluxes with Gaussian Models

Here we describe simple sanity checks of our measurements of enclosed fluxes in the ALMA clean component maps presented in Section 5. We prepared 100 independent noise data of ALMA visibility generated from actual ALMA data for ASXDF1100.053.1. We input a symmetric Gaussian model with a size into the 100 noise visibility data. Here a total flux of the input model is the same as that of ASXDF1100.053.1. We imaged and cleaned the 100 noise visibilities with the input model in the same manner as the actual observed data for ASXDF1100.053.1, and we measured enclosed fluxes. We repeated these process from input sizes of 0$''$.025 (FWHM) to 0$''$.800 with a step of 0$''$.025.

Figure 13 shows the resulting enclosed fluxes of mock Gaussian sources as a function of radius. The extracted fluxes of the mock sources show that the input total fluxes are recovered. However, in the cases of mock sources with larger input size, the input total fluxes are not completely recovered.

A fraction of flux remaining in a residual image is expected to increase in our clean process down to the 1σ noise level for a source with a larger size. At a mm-wave size of $\lesssim 0\farcs40$ where ASXDF1100.053.1 is located, the expected missing flux is $\lesssim 2\%$, which is negligible. We also conducted simulations using the ALMA data for ASXDF1100.231.1 and obtained results similar to those for ASXDF1100.053.1.

Figure 14 shows comparisons between input and output half-light radii from the simulations based on the ALMA data for ASXDF1100.053.1 and 231.1, respectively. Both plots indicate that our source size measurements in the ALMA continuum clean component maps are sensitive down to the limit by the pixel scale of $0\farcs05$ pixel^{-1}. Figure 14 indicates that source size measurements in the ALMA continuum clean component map of ASXDF1100.231.1 can reproduce sizes well. On the other hand, Figure 14 shows that size measurements in the ALMA continuum clean component map of ASXDF1100.053.1 can overestimate sizes around a size of ~0.10–0.15 arcsec. The overestimation of sizes can be at most ~0.02 arcsec, or 20%. However, the measured size ($R_{c,e}$) of ASXDF1100.053 is $0\farcs17$, therefore the possible systematic offset is not expected to contribute to the measured size of ASXDF1100.053.1.

References

Aretxaga, I., Hughes, D. H., Chapin, E. L., et al. 2003, MNRAS, 342, 759
Aretxaga, I., Hughes, D. H., Coppin, K., et al. 2007, MNRAS, 379, 1571
Aretxaga, I., Hughes, D. H., & Dunlop, J. S. 2005, MNRAS, 358, 1240
Aretxaga, I., Wilson, G. W., Aguilar, E., et al. 2011, MNRAS, 415, 3831
Arnouts, S., Cristiani, S., Moscardini, L., et al. 1999, MNRAS, 310, 540
Asboth, V., Conley, A., Sayers, J., et al. 2016, MNRAS, 462, 1989
Ashby, M. L. N., Willner, S. P., Fazio, G. G., et al. 2013, ApJ, 769, 80
Barro, G., Kriek, M., Pérez-González, P. G., et al. 2016, ApJL, 827, L32
Bell, E. F. 2003, ApJ, 586, 794
Belli, S., Newman, A. B., Ellis, R. S., & Konidaris, N. P. 2014, ApJL, 788, L29
Biggs, A. D., Ivison, R. J., Ibar, E., et al. 2011, MNRAS, 413, 2314
Blain, A. W., Smail, I., Ivison, R. J., Kneib, J.-P., & Frayer, D. T. 2002, PhR, 369, 111
Borys, C., Scott, D., Chapman, S., et al. 2004, MNRAS, 355, 485
Bruzual, G., & Charlot, S. 2003, MNRAS, 344, 1000
Calzetti, D., Armus, L., Bohlin, R. C., et al. 2000, ApJ, 533, 682
Capak, P. L., Riechers, D., Scoville, N. Z., et al. 2011, Natur, 470, 233
Caputi, K. I., Cirasuolo, M., Dunlop, J. S., et al. 2011, MNRAS, 413, 162
Caputi, K. I., Michalowski, M., Krips, M., et al. 2014, ApJ, 788, 126
Carilli, C. L., Hodge, J., Walter, F., et al. 2011, ApJL, 739, L33
Carilli, C. L., & Yun, M. S. 1999, ApJL, 513, L13
Chabrier, G. 2003, PASP, 115, 763
Chapman, S. C., Blain, A. W., Ivison, R. J., & Smail, I. R. 2003, Natur, 422, 695
Chapman, S. C., Blain, A. W., Smail, I., & Ivison, R. J. 2005, ApJ, 622, 772
Chary, R., & Elbaz, D. 2001, ApJ, 556, 562
Condon, J. J. 1992, ARA&A, 30, 575
Cowley, W. I., Lacey, C. G., Baugh, C. M., & Cole, S. 2015, MNRAS, 446, 1784
Cox, P., Krips, M., Neri, R., et al. 2011, ApJ, 740, 63
da Cunha, E., Groves, B., Walter, F., et al. 2013, ApJ, 766, 13
da Cunha, E., Walter, F., Smail, I. R., et al. 2015, ApJ, 806, 110
Dannerbauer, H., Walter, F., & Morrison, G. 2008, ApJL, 673, L127
Dowell, C. D., Conley, A., Glenn, J., et al. 2014, ApJ, 780, 75
Draine, B. T., Dale, D. A., Bendo, G., et al. 2007, ApJ, 663, 866
Furusawa, H., Kosugi, G., Akiyama, M., et al. 2008, ApJS, 176, 1
Geach, J. E., Dunlop, J. S., Halpern, M., et al. 2017, MNRAS, 465, 1789
Gear, W. K., Lilly, S. J., Stevens, J. A., et al. 2000, MNRAS, 316, L51
Harrison, C. M., Simpson, J. M., Stanley, F., et al. 2016, MNRAS, 457, L122
Hayward, C. C., Narayanan, D., Kereš, D., et al. 2013, MNRAS, 428, 2529
Hodge, J. A., Karim, A., Smail, I., et al. 2013, ApJ, 768, 91
Hodge, J. A., Swinbank, A. M., Simpson, J. M., et al. 2016, ApJ, 833, 103
Hughes, D. H., Aretxaga, I., Chapin, E. L., et al. 2002, MNRAS, 335, 871
Hughes, D. H., Serjeant, S., Dunlop, J., et al. 1998, Natur, 394, 241
Ikarashi, S., Ivison, R. J., Caputi, K. I., et al. 2015, ApJ, 810, 133
Ikarashi, S., Kohno, K., Aguirre, J. E., et al. 2011, MNRAS, 415, 3081
Ilbert, O., Arnouts, S., McCracken, H. J., et al. 2006, A&A, 457, 841
Iono, D., Peck, A. B., Pope, A., et al. 2006, ApJL, 640, L1
Iono, D., Yun, M. S., Aretxaga, I., et al. 2016, ApJL, 829, L10
Isobe, T., Feigelson, E. D., & Nelson, P. I. 1986, ApJ, 306, 490
Ivison, R. J., Greve, T. R., Dunlop, J. S., et al. 2007, MNRAS, 380, 199
Ivison, R. J., Greve, T. R., Smail, I., et al. 2002, MNRAS, 337, 1
Ivison, R. J., Lewis, A. J. R., Weiss, A., et al. 2016, ApJ, 832, 78
Ivison, R. J., Smail, I., Barger, A. J., et al. 2000, MNRAS, 315, 209
Ivison, R. J., Smail, I., Dunlop, J. S., et al. 2005, MNRAS, 364, 1025
Ivison, R. J., Smail, I., Le Borgne, J.-F., et al. 1998, MNRAS, 298, 583
Ivison, R. J., Swinbank, A. M., Swinyard, B., et al. 2010, A&A, 518, L35
Kennicutt, R. C., Jr. 1998, ARA&A, 36, 189
Krogager, J.-K., Zirm, A. W., Toft, S., Man, A., & Brammer, G. 2014, ApJ, 797, 17
Lawrence, A., Warren, S. J., Almaini, O., et al. 2007, MNRAS, 379, 1599
Lindner, R. R., Baker, A. J., Omont, A., et al. 2011, ApJ, 737, 83
Lutz, D., Berta, S., Contursi, A., et al. 2016, A&A, 591, A136
Mancuso, C., Lapi, A., Shi, J., et al. 2016, ApJ, 823, 128
McBride, J., Quataert, E., Heiles, C., & Bauermeister, A. 2014, ApJ, 780, 182
Messias, H., Dye, S., Nagar, N., et al. 2014, A&A, 568, A92
Murphy, E. J. 2009, ApJ, 706, 482
Oliver, S. J., Bock, J., Altieri, B., et al. 2012, MNRAS, 424, 1614
Oteo, I., Zwaan, M. A., Ivison, R. J., Smail, I., & Biggs, A. D. 2016, arXiv:1607.06464
Pope, A., Scott, D., Dickinson, M., et al. 2006, MNRAS, 370, 1185
Riechers, D. A., Bradford, C. M., Clements, D. L., et al. 2013, Natur, 496, 329
Rieke, G. H., Alonso-Herrero, A., Weiner, B. J., et al. 2009, ApJ, 692, 556
Silva, L., Granato, G. L., Bressan, A., & Danese, L. 1998, ApJ, 509, 103
Simpson, J. M., Smail, I., Swinbank, A. M., et al. 2015a, ApJ, 799, 81
Simpson, J. M., Smail, I., Swinbank, A. M., et al. 2015b, ApJ, 807, 128
Simpson, J. M., Swinbank, A. M., Smail, I., et al. 2014, ApJ, 788, 125
Smail, I., Ivison, R. J., & Blain, A. W. 1997, ApJL, 490, L5
Smail, I., Ivison, R. J., Kneib, J.-P., et al. 1999, MNRAS, 308, 1061
Smolčić, V., Aravena, M., Navarrete, F., et al. 2012, A&A, 548, A4
Smolčić, V., Karim, A., Miettinen, O., et al. 2015, A&A, 576, A127
Straatman, C. M. S., Labbé, I., Spitler, L. R., et al. 2015, ApJL, 808, L29
Strandet, M. L., Weiss, A., Vieira, J. D., et al. 2016, ApJ, 822, 80
Swinbank, A. M., Karim, A., Smail, I., et al. 2012, MNRAS, 427, 1066
Swinbank, A. M., Simpson, J. M., Smail, I., et al. 2014, MNRAS, 438, 1267
Toft, S., Smolčić, V., Magnelli, B., et al. 2014, ApJ, 782, 68
Umehata, H., Tamura, Y., Kohno, K., et al. 2014, NMRAS, 440, 3462
Vieira, J. D., Marrone, D. P., Chapman, S. C., et al. 2013, Natur, 495, 344
Walter, F., Decarli, R., Carilli, C., et al. 2012, Natur, 486, 233
Wang, W.-H., Barger, A. J., & Cowie, L. L. 2009, ApJ, 690, 319
Wardlow, J. L., Cooray, A., De Bernardis, F., et al. 2013, ApJ, 762, 59
Wardlow, J. L., Smail, I., Coppin, K. E. K., et al. 2011, MNRAS, 415, 1479
Weiß, A., De Breuck, C., Marrone, D. P., et al. 2013, ApJ, 767, 88
Weiß, A., Ivison, R. J., Downes, D., et al. 2009, ApJL, 705, L45
Younger, J. D., Fazio, G. G., Huang, J.-S., et al. 2007, ApJ, 671, 1531
Younger, J. D., Fazio, G. G., Huang, J.-S., et al. 2009, ApJ, 704, 803
Yun, M. S., Reddy, N. A., & Condon, J. J. 2001, ApJ, 554, 803
Yun, M. S., Scott, K. S., Guo, Y., et al. 2012, MNRAS, 420, 957
Zhang, Z.-Y., Papadopoulos, P. P., Ivison, R. J., et al. 2016, RSOS, 3, 160025